*J. Fluid Mech.* (2007), *vol.* 591, *pp.* 43–71.  
doi:10.1017/S0022112007008270 Printed in the United Kingdom

# Buoyancy-driven variable-density turbulence

D. LIVESCU AND J. R. RISTORCELLI
Los Alamos National Laboratory, Los Alamos, NM 87544, USA
livescu@lanl.gov; jrrj@lanl.gov

(Received 27 October 2006 and in revised form 6 July 2007)

Buoyancy-generated motions in an unstably stratified medium composed of two incompressible miscible fluids with different densities, as occurs in the variable-density Rayleigh–Taylor instability, are examined using direct numerical simulations. The non-equilibrium homogeneous buoyantly driven problem is proposed as a unit problem for variable density turbulence to study: (i) the nature of variable density turbulence, (ii) the transition to turbulence and the generation of turbulence by the conversion of potential to kinetic energy; (iii) the role of non-Boussinesq effects; and (iv) a parameterization of the initial conditions by a static Reynolds number. Simulations are performed for Atwood numbers up to 0.5 with root mean square density up to 50% of the mean density and Schmidt numbers, $0.1 \leqslant Sc \leqslant 2$. The benchmark problem has been designed to have the largest mass flux possible and is, in this configuration, the maximally unstable non-equilibrium flow possible. It is found that the mass flux, owing to its central role in the conversion of potential to kinetic energy, is probably the single most important dynamical quantity to predict in lower-dimensional models. Other primary findings include the evolution of the mean pressure gradient: during the non-Boussinesq portions of the flow, the evolution of the mean pressure gradient is non-hydrostatic (as opposed to a Boussinesq fluid) and is set by the evolution of the specific volume pressure gradient correlation. To obtain the numerical solution, a new pressure projection algorithm which treats the pressure step exactly, useful for simulations of non-solenoidal velocity flows, has been constructed.

## 1. Introduction

Many turbulent flows involve mixing between fluids with very different densities. Even if the fluids participating in the mixing are incompressible, the resulting velocity fields, owing to the change in the specific volume accompanying molecular mixing, are not divergence free. We refer to such flows as variable-density (VD) flows. VD flows occur in a variety of engineering applications such as the mixing of shear layers between two gases of different densities, e.g. hydrogen and oxygen, or buoyantly driven situations in which there is a body force that causes the interpenetration of two fluids as occurs in the Rayleigh–Taylor (RT) and Richtmyer–Meshkov instabilities (Cabot & Cook 2006). More complex flows involving combustion in low- or high-speed flows (scram and ramjets) fall into this class, as do many flows of chemical engineering interest (Givi 1989). Here, we consider a simple form of multimaterial mixing (Besnard *et al.* 1992) which involves two fluids with different densities for which the individual mass fractions can be recovered from the density.

The properties of the turbulence, when it has been studied in such flows, are usually obscured by the presence of inhomogeneities due to edge effects and/or walls. The current investigation focuses on the nonlinear dynamics and statistics of buoyantly

driven turbulence by considering the statistically homogeneous problem. As such, the effects of the new nonlinearities due to large density variations in the advective terms of the Navier–Stokes equations are studied in the absence of complicating inhomogeneities. The problem is an extension to the variable-density case of the buoyancy-generated turbulence in a Boussinesq fluid studied by Batchelor, Canuto & Chasnov (1992). The subject of this paper differs in several fundamental ways. Here, the high-Atwood-number variable-density problem, not the Boussinesq problem, is treated. Energy budgets for the second-moment equations and the effect of Schmidt number are also studied. A portion of the current problem is addressed, in fact, in Sandoval (1995). Like Sandoval, Clark & Riley (1996), Cook & Dimotakis (2001) and Ristorcelli & Clark (2004), our interest here is in the statistics of the fluctuating velocity field. In a companion paper (Livescu & Ristorcelli 2007), the focus will be on the scalar field and the material mixing.

The current paper treats low-speed flows in which the turbulent Mach number is small and the fluids participating in the mixing are incompressible. Owing to large density differences, the fluid is not amenable to the Boussinesq approximation, and the velocity field, unlike Batchelor *et al.* (1992), is not solenoidal. For such a flow, the term variable density (VD) is used to distinguish it from the Boussinesq approximation in which the densities of the fluids participating in the mixing are similar and density variations in the momentum equations, except in the buoyancy term, are negligible. The primary non-dimensional parameter characterizing variable-density effects is the Atwood number:

$$A = \frac{\rho_2 - \rho_1}{\rho_2 + \rho_1} \qquad \Rightarrow \qquad \frac{\rho_2}{\rho_1} = \frac{1 + A}{1 - A}, \tag{1}$$

where $\rho_2$ is the pure fluid density of the heavy fluid. The Atwood number ranges from 0 to 1. For air interpenetrating helium, for which the density ratio is $\rho_2/\rho_1 \approx 7$, the Atwood number is $A \approx 0.75$. For air and hydrogen, $A = 0.85$. Similar Atwood numbers occur for mixing between liquid hydrocarbons and air. In contrast, the Boussinesq approximation, for which the mean pressure gradient is hydrostatic, corresponds to $A \to 0$.

In VD buoyantly driven flows, unlike the Boussinesq approximation, the mean pressure gradient is a dynamically evolving quantity coupled to the mixing. In many turbulent flows of engineering interest, the mean velocity gradient is responsible for converting the kinetic energy of the mean flow to the turbulence. In the flow considered here, the primary production mechanism, for both the transitional and turbulent phases, is buoyancy, and kinetic energy is produced by conversion of potential energy by the mass flux, $\langle \rho u_i \rangle$, where $\rho$ and $u_i$ are density and velocity fluctuations and angle brackets denote the average. The mass flux is responsible for the conversion of potential energy to kinetic energy which in turn determines the mixing rate which feeds back to the mass flux. Since the mass flux dictates the energy conversion rate, it is also related to the growth of the RT mixing layer as observed by Cook, Cabot & Miller (2004). Thus, even if the mass flux makes a small contribution to the normal Favre Reynolds stresses, as is the case here, the mass flux is the keystone of the buoyantly driven variable-density flows. While 'mass flux' connotes advection of density, it should be kept in mind that in this flow the mean density gradient is zero and mass is advected.

The proposed buoyantly driven statistically homogeneous study is a unit problem for studying the additional cubic (as well as quadratic) nonlinearities in the Navier–Stokes equations and the mixing arising from the strong coupling of velocity and

density fluctuations. The fluid physics we investigate occur, more generally, in rapidly accelerating flows composed of different density fluids. It is, in all such cases, the mean pressure gradient that drives the turbulence and the mixing.

The moment equations for this problem are, except for the inhomogeneous flux terms, identical to those describing turbulence in the RT mixing layer. Summaries of RT simulation studies can be found in the overviews of Dalziel, Linden & Youngs (1999) and Young *et al.* (1999) and references therein. Additional commentary may be found in Ristorcelli & Clark (2004). The inhomogeneous RT transport terms are important at the edge of the layer and thus, in principle, the current homogeneous simulations describe the core of a fully developed (wide) RT layer after a time at which enough mixing occurs such that little pure fluid attains the centreline. This can be inferred by inspection of the centreline density kurtosis given in Ristorcelli & Clark (2004). In addition, the current simulations contain the essential nonlinear features of the RT problem that give rise to: (i) the cascade of energy; (ii) the conversion of potential to kinetic energy by the mass flux; (iii) the decrease of the mean specific volume by mixing; and (iv) the increase of the integral length scale. The simulations have been motivated by the absence of data relevant to moment closures or large-eddy simulation (LES) developments in VD turbulence that capture the core of the nonlinear coupling between material mixing and the hydrodynamical field in the absence of the complicating issues of spatial transport. From an engineering point of view, any model for the turbulence and mixing in general variable-density flows must be capable of simulating the dynamics of this simple buoyantly driven VD turbulence.

### 1.1. *Highlights of this study*

In this paper, we look for and describe new physics that might be seen in VD turbulence. As such, this paper is to be considered exploratory in intent: there is simply not much known about VD turbulence. Our study contributes to several important areas.

(*a*) A study of the mass flux and the role it plays in the conversion of potential energy to kinetic energy.

(*b*) That the mean pressure gradient is, in VD turbulence, a dynamically evolving quantity that is coupled to the mixing as manifests itself in its Schmidt-number dependence.

(*c*) The identification of a static or initial buoyancy Reynolds number that parameterizes the initial conditions of this flow as well as the RT problem.

(*d*) An improved numerical algorithm for non-solenoidal flows due to active scalar mixing.

In addition to insights into the physics of VD turbulence, an archival database is provided to test reduced degree-of-freedom models. The material mixing in this flow is treated in a companion paper (Livescu & Ristorcelli 2007).

### 1.2. *Plan of the paper*

The first portion of the paper sets up the DNS problem and then also shows that, owing to homogeneity, there is a non-uniqueness to the problem. This is solved by choosing a mean volumetric velocity such that growth of the mass flux is maximized. A discussion of the initial conditions and attendant details is then given. The longest results section, §4, focuses on the diagnostic metrics of the flow. Issues related to its VD nature, its highly non-equilibrium characteristics, the Reynolds numbers, and the potential to kinetic energy conversion are amplified.

## 2. Problem formulation

The governing equations, special strategies necessary for the numerical solution, and well-posedness issues are presented. In resolving the well-posedness issues, the mean velocity is chosen to maximize the mass flux. Therefore the simulations presented, as explained below, represent the maximally non-equilibrium flow.

### 2.1. *Governing equations*

The physical problem is the mixing of two incompressible fluids with different densities, $\rho_1$ and $\rho_2$. The mathematical model is provided by the Navier–Stokes equations and species mass fraction transport equations. The density of the mixture varies depending on the amount of each fluid in the mixture:

$$\rho = \frac{1}{Y_1/\rho_1 + Y_2/\rho_2}, \tag{2.1}$$

where $Y_1 = Y_1(\boldsymbol{x}, t)$ and $Y_2 = Y_2(\boldsymbol{x}, t)$ are the mass fractions, and $Y_1 + Y_2 = 1$. The species mass fraction transport equations, assuming Fickian diffusion, are:

$$(\rho Y_\alpha)_{,t} + (\rho Y_\alpha u_j)_{,j} = (\rho D_0 Y_{\alpha,j})_{,j}. \tag{2.2}$$

Summing over $\alpha = 1, 2$, leads to the continuity equation (see below). The change in the specific volume, $1/\rho$, owing to mixing, leads to non-zero divergence of velocity:

$$u_{j,j} = -D_0 \ln \rho_{,jj} \tag{2.3}$$

which can be derived from (2.1)–(2.2) (see Sandoval 1995; Cook & Dimotakis 2001). $D_0$ is the diffusion coefficient and is assumed constant.

After non-dimensionalizing with $\rho_0 = 0.5(\rho_1 + \rho_2)$, a reference velocity, $U_0$, and a reference length, $L_0$, the governing equations become:

$$\rho^*_{,t} + (\rho^* u^*_j)_{,j} = 0, \tag{2.4}$$

$$(\rho^* u^*_i)_{,t} + (\rho^* u^*_i u^*_j)_{,j} = -p^*_{,i} + \tau^*_{ij,j} + \frac{1}{Fr^2}\rho^* g_i, \tag{2.5}$$

$$u^*_{j,j} = -\frac{1}{Re_0 Sc} \ln \rho^*_{,jj}, \tag{2.6}$$

with $\tau^*_{ij} = (1/Re_0)(u^*_{i,j} + u^*_{j,i} - (2/3)u^*_{k,k}\delta_{ij})$. Note that VD introduces additional nonlinearities in the governing equations besides the quadratic terms present in constant density Navier–Stokes equations. There are new cubic terms in the momentum equations and the divergence of velocity in terms of the logarithm of the density.

The primary dependent variables are the density $\rho^*$, velocity in the $x_i$-direction $u^*_i$, and pressure $p^*$. The superscript $^*$ is used to denote total instantaneous (mean plus fluctuation) values. The non-dimensional parameters in (2.4)–(2.6) are the computational Reynolds number, $Re_0$, Schmidt number, $Sc$, and Froude number, $Fr$:

$$Re_0 = \rho_0 L_0 U_0/\mu_0, \tag{2.7}$$

$$Sc = \mu_0/\rho_0 D_0, \tag{2.8}$$

$$Fr^2 = U_0^2/gL_0, \tag{2.9}$$

with $g$, the magnitude of the acceleration due to gravity, taken to be constant. Here, $g_i$ are the components of the unit vector in the direction of gravity. In the above non-dimensionalization, the reference scales $L_0$ and $U_0$ are not specified. A physically meaningful choice, which collapses the data will be provided later. The

dynamic viscosity $\mu_0$ is assumed constant and is the same for both fluids. In the equations above, the non-dimensional instantaneous density varies between $1 - A(t)$ and $1 + A(t)$ where $A(t)$ is the instantaneous Atwood number.

Equations (2.4)–(2.6) are those governing the flow generated by the VD RT instability (e.g. see Sandoval 1995; Cook & Dimotakis 2001). In this study, the equations are solved in a triply periodic domain, corresponding to a statistically homogeneous flow. Consistently, the averages are calculated as volume averages. Such a configuration eliminates the complications due to the presence of non-periodic boundaries while allowing fundamental studies of turbulence with buoyancy and VD effects in the context of mixing between initially segregated materials. Physically, the flow corresponds to the inner region of a fully developed RT mixing layer. For modelling, this is a benchmark problem which any turbulence model for the VD RT should handily predict. In flow physics this benchmark problem allows us to study the peculiar nature of the mixing between two different density fluids. There are several phenomena that distinguish the VD fluid from a Boussinesq fluid. These differences are highlighted throughout the text and in the Appendix.

In the subsequent sections capital roman letters, overbars and angle brackets are used to denote mean values. Angle brackets are preferred for longer expressions whereas overbars are used for quantities denoted by Greek letters. Lower case letters (Roman or Greek) or primes are used to denote fluctuations. As the density is not spatially uniform, some of the results will be presented using density-weighted (Favre) averages, denoted with a tilde, and the corresponding fluctuations with double primes. Thus, the instantaneous velocity, density, pressure and specific volume are decomposed as $u_i^* = U_i + u_i = \tilde{U}_i + u_i''$, $\rho^* = \overline{\rho} + \rho$, $p^* = P + p$ and $v^* = V + v$, respectively. Note that $\tilde{U}_i - U_i = u_i - u_i'' = a_i$. The definitions for the normalized mass flux, $a_i$, Favre Reynolds stresses, $R_{ij}$, and turbulent kinetic energy, $\tilde{k}$, and total kinetic energy, $E_K$, are given below:

$$a_i = \frac{\langle u_i \rho \rangle}{\bar{\rho}} = -\langle u_i'' \rangle, \tag{2.10}$$

$$R_{ij} = \langle \rho^* u_i'' u_j'' \rangle = \bar{\rho} \langle u_i u_j \rangle - \bar{\rho} a_i a_j + \langle \rho u_j u_j \rangle, \qquad R_{kk} = 2\bar{\rho}\tilde{k}, \tag{2.11}$$

$$E_K = \langle \rho^* u_i^* u_i^* \rangle / 2. \tag{2.12}$$

In this homogeneous VD flow, as will be shown, the mean velocity is zero. Unlike constant-density flows, the two first-order moments, the mean pressure gradient, $P_{,i}$, and the mean specific volume, $V$, are dynamical variables evolving as the mixing proceeds.

### 2.2. *Well-posedness and the mean pressure gradient*

The governing equations are translationally invariant. As a consequence, any statistical quantity formed from the dependent variables is invariant under translation and the flow remains statistically homogeneous if the initial conditions are consistent with the periodic boundary conditions. To solve the equations, the pressure is determined from a Poisson equation (see Appendix A). Because of periodicity, the mean pressure gradient is determined only up to an arbitrary constant. As a consequence, $\nabla P$ is a dynamical variable to which an arbitrary constant can be added. Note that the addition of a constant mean pressure gradient to the momentum equations does not change its translational invariance. All other statistics are constant in space, consistent with statistical homogeneity.

Given that $\nabla P$ can be determined to an arbitrary constant, the question is what is the mean pressure gradient which gives the maximally unstable turbulence? Two constraints are imposed to fix the mean pressure gradient: (i) that for each direction $i$, $g_i U_{i,t} \geqslant 0$ and (ii) the time derivative of the mass flux attains its maximum absolute value. The potential is converted to kinetic energy by the mass flux (as will be shown). Therefore, the second constraint ensures the fastest energy conversion and the flow obtained will be the most non-equilibrium flow possible.

Mathematically, the first constraint requires that the first and last terms in the equation

$$U_{i,t} = \langle u_i u_{j,j} \rangle - \langle v p_{,i} \rangle + \langle v \tau_{ij,j} \rangle - V P_{,i} + \frac{1}{Fr^2} g_i \tag{2.13}$$

have the same sign. In other words, the mean velocity magnitude cannot decrease if it is generated by buoyancy.

The second constraint requires that the time derivative of the mass flux

$$\langle \rho u_i \rangle_{,t} = -\langle \rho v \rangle P_{,i} - \overline{\rho}(\langle u_i u_{j,j} \rangle - \langle v p_{,i} \rangle + \langle v \tau_{ij,j} \rangle) \tag{2.14}$$

attains its maximal absolute value, $|\langle \rho u_i \rangle_{,t}| = |\langle \rho u_i \rangle_{,t}|_{max}$.

Equation (2.13) is the average of the instantaneous velocity equation

$$u^*_{i,t} = -u_j u_{i,j} - \frac{1}{\rho^*}(p_{,i} + P_{,i} - \tau_{ij,j}) + \frac{1}{Fr^2} g_i, \tag{2.15}$$

which is obtained from (2.5) after dividing by $\rho^*$ and applying the Reynolds decomposition. Integration by parts and homogeneity were used to obtain the first term on the right-hand side of (2.13). Equation (2.14) is derived from (2.5) after decomposing $\rho^* = \overline{\rho} + \rho$, eliminating $(\overline{\rho} u_i)_{,t}$ with the use of the continuity equation (2.4) and (2.15), and taking the average.

The two constraints above determine the mean pressure gradient. First, note that the averaged continuity equation is $\overline{\rho}_{,t} = 0$ and $\overline{\rho} = 1$. The Schwartz inequality requires:

$$\left(\frac{1}{\mathcal{V}} \int_{\mathcal{V}} \rho^* \, \mathrm{d}\mathcal{V}\right)^{1/2} \left(\frac{1}{\mathcal{V}} \int_{\mathcal{V}} \frac{1}{\rho^*} \, \mathrm{d}\mathcal{V}\right)^{1/2} \geqslant \frac{1}{\mathcal{V}} \int_{\mathcal{V}} (\rho^*)^{1/2} \left(\frac{1}{\rho^*}\right)^{1/2} \mathrm{d}\mathcal{V} = 1, \tag{2.16}$$

which shows that $\overline{\rho} V \geqslant 1$ and thus $\langle \rho v \rangle = 1 - \overline{\rho} V \leqslant 0$. Set $P_{,i} = 1/V(\langle u_i u_{j,j} \rangle - \langle v p_{,i} \rangle + \langle v \tau_{ij,j} \rangle + 1/Fr^2 g_i - \epsilon_i)$. Here, $\epsilon_i$ is the unknown time derivative of the mean velocity, $U_{i,t}$, and can have positive or negative values. The right-hand side of the mean velocity equation (2.13) can have the sign of $g_i$ only when $\epsilon_i g_i \geqslant 0$ (no summation over $i$). From constraint (ii), since $\langle \rho v \rangle \leqslant 0$, we find that $\epsilon_i g_i \leqslant 0$ (no summation), which leaves only $\epsilon_i = 0$. The mean pressure gradient that satisfies the two constraints can only be:

$$P_{,i} = \frac{1}{V}\left(\frac{1}{Fr^2} g_i - \langle v p_{,i} \rangle + \langle u_i u_{j,j} \rangle + \langle v \tau_{ij,j} \rangle\right), \tag{2.17}$$

and $U_{i,t} = 0$. The first two terms dominate the right-hand side of (2.17); thus the VD deviation of the pressure gradient from hydrostatic is set by the specific volume pressure gradient correlation. The same mean pressure gradient was used by Sandoval *et al.* (1996). Equation (2.17) shows that, unlike the Boussinesq case, the mean pressure is a dynamical quantity. For an RT flow, the mean pressure gradient is set by the non-periodic boundary conditions and, for the VD case, is a dynamical quantity changing with the mixing. $U_{i,t} \approx 0$ also occurs in the high-Reynolds VD RT simulation of Cabot & Cook (2006) so that the maximally unstable configuration chosen here is

close to the RT situation. For the triply periodic case, we could, in principle, choose a mean velocity such that the mean pressure gradient is equal to the hydrostatic pressure head. In this case, which corresponds to a less non-equilibrium flow, the mean velocity is not constant, but a dynamical variable changing with the mixing.

The Galilean invariance of the governing equations allows a reference frame moving with any constant velocity to be chosen. Choosing $U_i = 0$ requires the following constraint between the mean and fluctuating momentum

$$\begin{aligned} 0 = U_i &= \left\langle \frac{\rho^* u_i^*}{\rho^*} \right\rangle = V\langle \rho^* u_i^* \rangle + \langle v(\rho^* u_i^*)' \rangle \\ &= V\langle \rho^* u_i \rangle + \langle v(\rho^* u_i)' \rangle, \end{aligned} \tag{2.18}$$

which must be satisfied as the equations are numerically integrated.

In summary, the governing equations describing VD buoyantly driven turbulence are (2.4)–(2.5) with $U_i = 0$, $u_i^* = u_i$ and the mean pressure gradient given by (2.17). The mean pressure gradient appears in the instantaneous pressure term in (2.5).

## 3. Numerical approach

Equations (2.4)–(2.5) are solved in a triply periodic domain using a pseudo–spectral algorithm. The derivatives are calculated in Fourier space and the nonlinear terms evaluated in real space. The numerical algorithm follows that described in Sandoval (1995) with differences discussed below and detailed in Appendix A. The equations are integrated in time using a second-order Adams–Bashforth method. In order to impose the condition $U_i = 0$ at each time step, the fluctuating momentum equation (A 2) is time integrated and at each time step the mean momentum, $\langle \rho^* u_i \rangle$, is calculated from (2.18). In contrast, Sandoval (1995) integrates both the fluctuating and the mean momentum equation, which enforces the condition $U_i = 0$ only to the order of the method.

The momentum equations (A 2) are time advanced using the pressure projection method in two steps: first without the pressure terms and then adding these terms to restore the correct divergence of velocity. For the incompressible case, it can be shown (see Karniadakis, Israeli & Orszag 1991) that the temporal treatment of the projection step is exact and the temporal accuracy of the overall method is determined by the first step. Because of the non-zero divergence of velocity, the pressure equation contains unknown terms which must be evaluated at the next time step. This problem occurs in all VD flows and was also encountered in the RT configuration (Cook & Dimotakis 2001). To close these unknown terms, usually (Sandoval 1995; Cook & Dimotakis 2001; Jang & de Bruyn Kops 2007) a second-order extrapollation of data from previous time steps is used. Such an approximation introduces additional errors in the velocity field and could, in principle, constrain the overall order of accuracy or affect the mass conservation. An equation for pressure which does not require further approximations, and ensures that the divergence equation (2.6) is exactly satisfied, is derived in Appendix A.

The evaluation of the nonlinear terms in real space introduces aliasing errors; these errors are controlled in two ways. First, by removing the energy in the wavenumbers $k \geqslant N/3$ where $N$ is the number of grid points. This completely eliminates the aliasing errors for quadratic products. For the other nonlinearities present in the governing equations, the aliasing errors are controlled by ensuring that the amount of energy in the wavenumbers affected by aliasing is small.

| Case | $A$ | $1/Fr^2$ | Sc | $Re_0$ | $Re_{b_0}$ | $\frac{\langle\rho^2\rangle}{\bar{\rho}^2}\|_{t=0}$ | Resolution |
|---|---|---|---|---|---|---|---|
| 1Base | 0.05 | 1.0 | 1.0 | 250 | 11 | 0.0024 | $256^3$ |
| 1Fr | 0.05 | 10.0 | 1.0 | 250 | 35 | 0.0024 | $256^3$ |
| 1Re1 | 0.05 | 1.0 | 1.0 | 833 | 37 | 0.0024 | $256^3$ |
| 1Re2 | 0.05 | 1.0 | 1.0 | 1667 | 73 | 0.0024 | $512^3$ |
| 2Sc0 | 0.25 | 1.0 | 0.1 | 250 | 26 | 0.057 | $256^3$ |
| 2Sc1 | 0.25 | 1.0 | 0.5 | 250 | 26 | 0.057 | $256^3$ |
| 2Base | 0.25 | 1.0 | 1.0 | 250 | 26 | 0.057 | $256^3$ |
| 2Sc2 | 0.25 | 1.0 | 2.0 | 250 | 26 | 0.057 | $256^3$ |
| 2Re1 | 0.25 | 1.0 | 1.0 | 833 | 87 | 0.06 | $512^3$ |
| 2Re2 | 0.25 | 1.0 | 1.0 | 1667 | 174 | 0.061 | $1024^3$ |
| 3Sc1 | 0.5 | 1.0 | 0.5 | 250 | 37 | 0.22 | $256^3$ |
| 3Base | 0.5 | 1.0 | 1.0 | 250 | 37 | 0.22 | $256^3$ |
| 3Sc2 | 0.5 | 1.0 | 2.0 | 250 | 37 | 0.22 | $512^3$ |

TABLE 1. parameters for the DNS cases.

### 3.1. *Initial conditions and simulation cases*

The density field is initialized as random blobs of pure fluids. First, a Gaussian random field with top-hat energy spectrum is generated. The location of wavenumbers with non-zero energy, $k_{min} \leqslant k \leqslant k_{max}$, is used to control the initial length-scale of the density field. For the cases considered $k_{min} = 3$ and $k_{max} = 5$, so that the flows starts with relatively large density structures. The density field is transformed into physical space where all negative values are set to the normalized density of the light fluid, $\rho_1/\rho_0$, and all positive values to the normalized density of the heavy fluid, $\rho_2/\rho_0$. The result is a field with mean 1 and double-delta PDF (Eswaran & Pope 1988; Livescu, Jaberi & Madnia 2002) which is smoothed by applying a filter function to decrease high wavenumber amplitudes. The physical values of the density are no longer bounded by $\rho_1/\rho_0$ and $\rho_2/\rho_0$ and, in order to reduce the difference between the maximum and minimum values, the field is allowed to go through pure molecular diffusion before the simulation is started. Thus, a thin diffusion layer is generated between the two fluids, as can be seen in figure 1, which ensures that all spatial scales can be accurately solved.

The velocity field is initialized with a zero solenoidal part and dilatational part given by gradients of the density field:

$$u_i = -\frac{1}{Re_0 Sc}(\ln \rho^*)_{,i} \tag{3.1}$$

which satisfies (2.6). Table 1 provides relevant information for the cases studied. For all cases $\boldsymbol{g} = (0, 0, -1)$. Two Reynolds numbers are given, $Re_0$ and a static buoyancy Reynolds number $Re_{0b}$ formed from an effective velocity related to the buoyancy forces and the initial integral scale of the density field. $Re_0$ is a non-dimensional viscosity as it is changed by changing $\mu_0$. The static buoyancy Reynolds number expresses the ratio of buoyancy and viscous forces at the time $g$ is applied and at a scale equal to the initial integral scale of the density field, as the velocity is calculated based on the potential energy corresponding to a height equal to the density integral scale. The dimensional potential velocity is $\sqrt{L_{0_\rho} Ag}$, with $L_{0_\rho}$ the dimensional initial

density integral scale, so that

$$Re_{b_0} = \frac{\rho_0 \sqrt{L_{0_\rho}^3 Ag}}{\mu_0} = Re_0 \sqrt{L_\rho^3 A/Fr^2}, \tag{3.2}$$

where $L_\rho = L_{0_\rho}/L_0$. In general, as will be seen, the higher $Re_{b0}$, the larger the maximum kinetic energy of the flow generated.

The cases described in table 1 were chosen to investigate the influence of the Atwood, Reynolds, Schmidt and Froude numbers. There are 3 base cases (1Base, 2Base, 3Base) corresponding to the Atwood numbers 0.05 (Boussinesq limit), 0.25 and 0.5. The rest of the cases have one value of the parameters *Sc*, *Re* and Froude numbers changed compared to the base cases. Cases with the same last number in the name have the same value of the respective changed parameter (i.e. both cases 1Re1 and 2Re1 have $Re_0 = 833$). In addition, the Froude number was changed for case 1Fr to match $A/Fr^2$ from case 3Base. To reduce statistical variability, each simulation is repeated several times with initial conditions generated using a different random number seed. All data presented represent averages over several realizations (typically 5 to 10). Because of the computational expense, the high-Reynolds-number cases 1Re2 and 2Re2 were computed only up to the kinetic energy maxima.

## 4. Results

### 4.1. *Overview of flow evolution*

The initial velocity field is very small magnitude as it is set by the dilatational field. The dilatational velocity, which is set by the smoothness of the density field, is small for the simulations considered. Because of the body force the two fluids move in opposite directions. Small- and large-scale fluctuations in the velocity and density fields are generated by nonlinear interactions and the fluids in contact molecularly mix. The amplification of the fluctuating strain field due to buoyancy increases the interfacial area between the two fluids (figure 2*a*) and the molecular mixing is accelerated. As the fluids become molecularly mixed, the viscous forces overcome the buoyancy forces and the turbulence begins to decay. At some late time (figure 2*b*) only the relatively large-scale regions survive; the small-scale density fluctuations have been smoothed out by molecular diffusion. Buoyancy forces still feed the slowly decaying large-scale components of the motions, but not enough to overcome the viscous forces and the turbulence decays.

Figure 3 shows the evolution of the kinetic energy $E_K = \langle \rho^* u_i u_i \rangle / 2$ and summarizes energetically the birth, growth and decay of buoyantly driven turbulence. The kinetic energy increases initially as buoyancy forces dominate viscous forces. As the fluids molecularly mix and the effective Atwood number decreases, the kinetic energy decays. To compare different cases, the results are plotted in terms of velocity and time scales characterizing the balance between buoyancy and nonlinear forces:

$$U_r = \sqrt{AgL_0}/U_0 = \sqrt{A/Fr^2}, \tag{4.1}$$

$$t_r = \sqrt{L_0/(Ag)}/(L_0/U_0) = \sqrt{Fr^2/A}. \tag{4.2}$$

Note that the corresponding dimensional scaling ($U_{0_r} = \sqrt{AgL_0}$ and $t_{0_r} = \sqrt{L_0/(Ag)}$) does not specify $L_0$, consistent with the absence of an intrinsic length scale in homogeneous flows. For quantitative comparisons with dimensional experiments, the

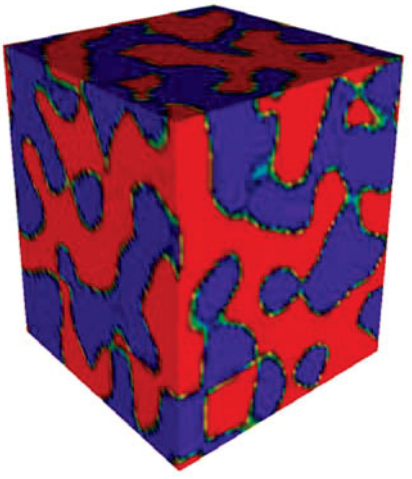

FIGURE 1. Typical initial density field.

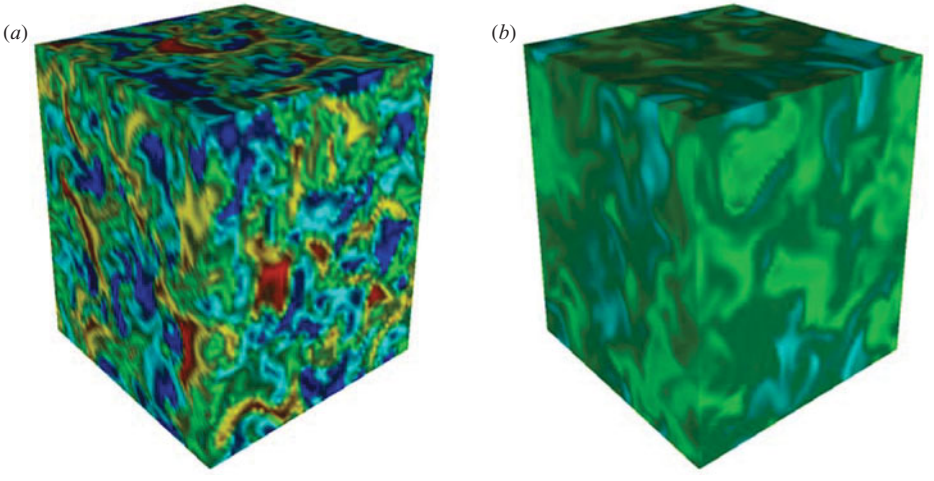


FIGURE 2. Typical density field at (*a*) maximum kinetic energy and (*b*) late time.

experimental length scale can be chosen to match a certain quantity (e.g. the density integral scale or Taylor microscale). The scaling above collapses the data better than the scaling based on the linear stability problem used by Ristorcelli & Clark (2004). The scales used here are similar to those used by Batchelor *et al.* (1992) with $A$ replacing the initial magnitude of the density fluctuations. Note that the present simulations have similar initial density length scales with only small differences due to the smoothing of the initial density field performed by diffusion.

Figure 3 shows that the buoyancy forces are larger for higher initial Atwood and Schmidt numbers or lower Froude numbers, resulting in larger kinetic energy maxima. For cases 1Fr and 3Base with the same initial $Re_{b_0}$, the results are close. Conversely, for cases with higher $Re_0$ (1Re1, 1Re2, 2Re1, 2Re2), the viscous forces are initially lower and the kinetic energy increases faster and has larger maxima. The growth of turbulence and the magnitude of the maxima correlate well with the initial buoyancy to viscous force balance, i.e. $Re_{b_0}$, as can be seen in a plot of the peak $E_K$

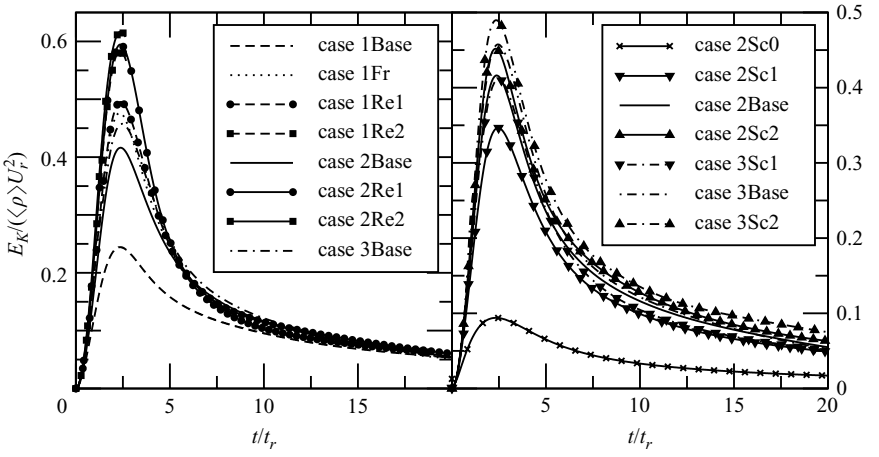


FIGURE 3. Time evolution of the turbulent kinetic energy.

versus $Re_{b_0}$ (not shown). In addition, the results seem to indicate that the maximum $E_K$ asymptotes to a constant as $Re_{b_0}$ increases; at larger $Re_{b_0}$, the change in the magnitude of the peak is progressively smaller, consistent with the Reynolds-number effect found in the largest RT simulation to date of Cabot & Cook (2006). The kinetic energy maxima occur at approximately the same non-dimensional time for all cases ($\approx$2.5). Figure 3(*b*) shows, as might be expected, that the higher $Sc$ cases produce a higher maximum and, unexpectedly, the maximum still peaks at the same time. At late times, the results obtained are similar for cases with $Sc = 1$. It is likely that the late time decay depends on the initial spectrum of the density field (and in particular its low-wavenumber component), as in the Boussinesq case (Batchelor *et al.* 1992).

Since buoyancy production is inherently anisotropic, it is expected that the normal stresses will be anisotropic. A measure of the large-scale anisotropy is the Reynolds stress anisotropy tensor:

$$b_{ij} = \frac{\langle \rho^* u_i u_j \rangle}{\langle \rho^* u_k u_k \rangle} - \tfrac{1}{3}\delta_{ij}, \tag{4.3}$$

which is bounded by $-1/3 \leqslant b_{ij} \leqslant 2/3$. The lower bound for a diagonal component corresponds to no energy in that component and the upper bound, 2/3, to 100% of the energy in that component. Similar to the RT runs of Ristorcelli & Clark (2004), the off-diagonal components of anisotropy tensor are zero. Parenthetically, the Boussinesq eddy-diffusivity closure of the standard $k-\epsilon$ model cannot predict buoyantly driven flows (Ristorcelli & Livescu 2007).

The vertical component $b_{33}$ of the anisotropy tensor is shown in figure 4. The initial dilatational velocity field is isotropic and $b_{33} = 0$ at $t = 0$. Since the gravitational force is applied suddenly at $t = 0$, $b_{33}$ rapidly increases as the solenoidal velocity is generated. At $t/t_r = 0.2$, more than 80% of the kinetic energy is in the vertical component. This is in the range of values obtained for the Boussinesq case by Batchelor *et al.* (1992) and slightly less than in the Boussinesq RT simulations of Ristorcelli & Clark (2004). As the turbulent fluctuations increase, the pressure strain redistributes the energy among the other normal stresses. In proportion, more energy is dissipated from $R_{33}$ by $\epsilon_{33}$ (not shown). Here, $\epsilon_{33}$ is the dissipation rate of $R_{33}$. Although the mass flux, generating $R_{33}$, still increases, the rate of growth is reduced by mixing and is not enough to compensate for the losses (by pressure strain and dissipation,

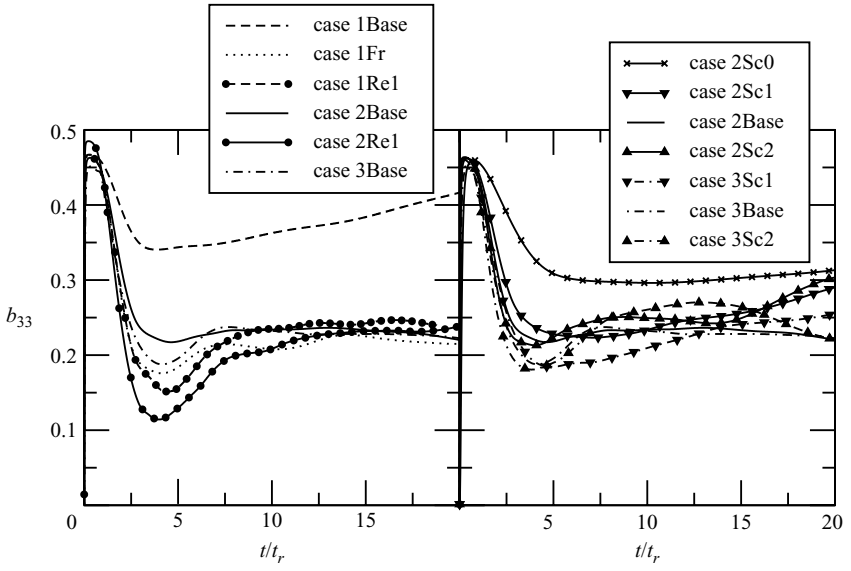


FIGURE 4. Vertical component of the anisotropy tensor.

see (4.8) below). Consequently, the anisotropy decreases. Later, although there is some statistical variability in the results, $b_{33}$ seems to asymptote to a constant value, $b_{33} \sim 0.25$ indicating that about 58% of the kinetic energy resides in the vertical component. For case 1Base, with the lowest Atwood and Reynolds numbers, the asymptotic value is similar to the results obtained for the homogeneous Boussinesq case (Batchelor *et al.* 1992). However, case 1Base does not appear to be turbulent as additional aspects to be shown also suggest. Although the statistical variability is larger for the higher $Sc$ cases, the results suggest that the asymptotic value of $b_{33}$ is larger at smaller Schmidt numbers. This is consistent with the faster decrease in the density contrast at smaller $Sc$ (Livescu & Ristorcelli 2007).

Unlike the kinetic energy, the root mean square (r.m.s.) density fluctuations only decrease in time. The density intensity defined as the r.m.s. density divided by the mean density is given in figure 5. The density intensity indicates the importance of non-Boussinesq effects (and the cubic nonlinearity) to the advective derivative. As explained in the Appendix, the Boussinesq approximation is obtained as $\rho/\overline{\rho} \to 0$. If $\rho_{rms}/\langle\rho\rangle < 0.05$ is taken to define the Boussinesq limit, then the low-Atwood-number cases 1Base, 1Fr, 1Re1 and 1Re2 are in this limit from the beginning. The other cases become Boussinesq-like after the kinetic energy peaks. The non-Boussinesq effects last longer for cases with higher $Re_{b_0}$ or $Sc$. If the density r.m.s. is scaled by the initial value, the long time values collapse for cases with the same $Sc$ when plotted against $t/t_r$, so that $Sc$ becomes the only parameter that affects the asymptotic state (not shown). The intermediate time (non-Boussinesq) behaviour depends in addition on $Re_{b_0}$.

In the Boussinesq case, the mean pressure gradient is constant in time and equal to the hydrostatic head $(1/Fr^2)\overline{\rho}g_i$. In the VD case, the mean pressure is a dynamical quantity and evolves as the mixing progresses, as seen in figure 6 and indicated by (2.17). As the mixing evolves and $\rho/\bar{\rho} \to 0$, $V \to 1/\bar{\rho}$, the mean pressure becomes hydrostatic. For all the cases considered, the last two terms in (2.17) are the largest. Thus, the specific volume pressure gradient correlation, $\langle vp_{,i}\rangle$, is primarily responsible for the non-Boussinesq behaviour of the mean pressure gradient as observed by

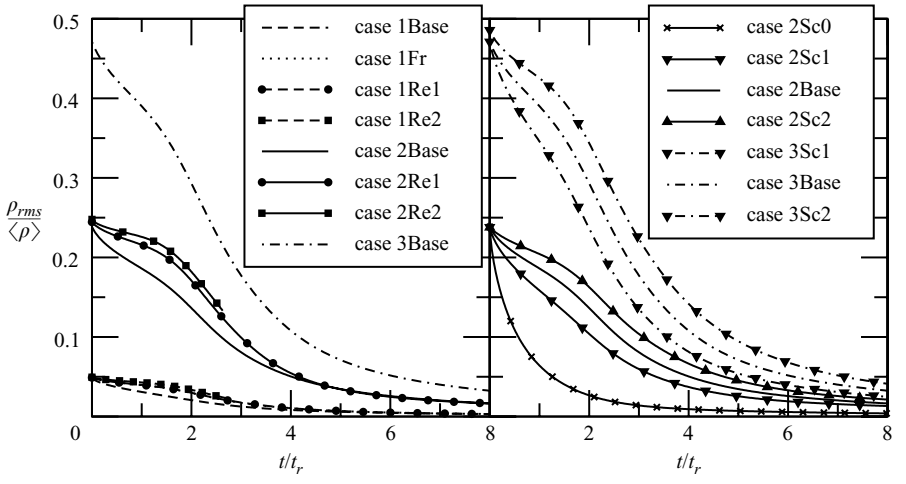


FIGURE 5. Time variation of the density intensity.

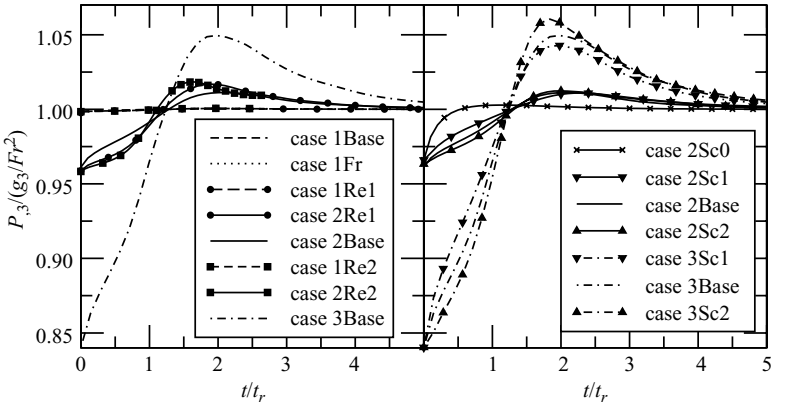


FIGURE 6. Time evolution of the mean pressure gradient normalized by the pressure head.

Sandoval *et al.* (1996). After the initial moment, most of energy resides in the solenoidal component (see below) and the pressure plays a role similar to that in incompressible flows: it reduces the velocity magnitude in the direction driven by gravity by transferring energy to the other two components. The pressure gradient is positive in the rising low-density regions and negative in the falling high-density regions. Since the specific volume is negatively correlated to the density, it yields that $\langle vp_{,i}\rangle > 0$ (see also § 4.5), and thus in the VD case it increases the pressure head. At early times when $V$ is largest, the specific volume is larger than 1 and the mean pressure gradient (2.17) is lower than the hydrostatic value. Later, as $V$ decreases, the mean pressure gradient becomes larger than the hydrostatic head. $P_{,3}$ crosses the hydrostatic pressure value for all cases at about the same time, and before the kinetic energy peaks.

Figure 6 indicates that non-Boussinesq effects are strongly dependent on Atwood number. Further increase in the non-Boussinesq effects can be obtained by increasing $Re_0$ or $Sc$. The current simulations have only moderate Atwood and Schmidt numbers owing to the large computational resources required to resolve high-Atwood and/or high- $Sc$ number cases. Even so, the r.m.s. density reaches 50% of the mean density, showing clear non-Boussinesq effects. Based on the results presented, we conclude

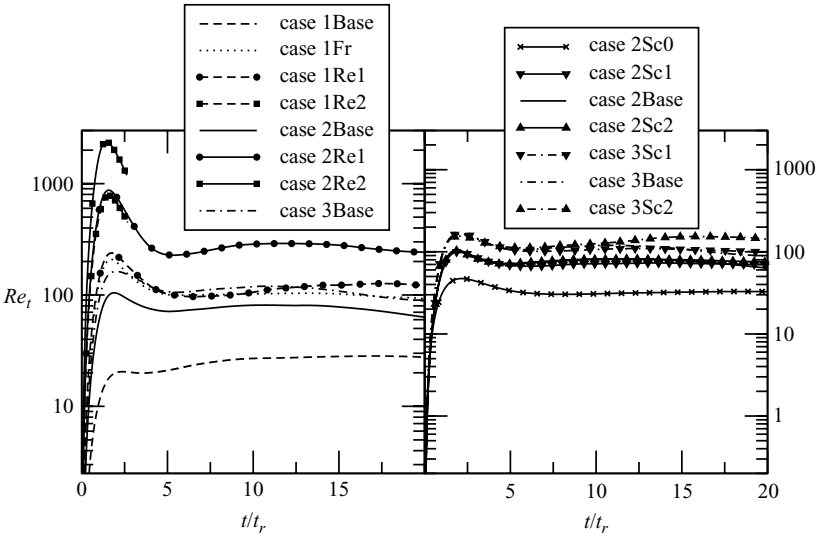


FIGURE 7. Time evolution of $Re_t$.

that non-Boussinesq effects, only modestly important at this Atwood number and for these initial conditions, will be especially important at higher Atwood and Schmidt numbers.

The turbulent Reynolds number, an indicator of the relative magnitude of the nonlinear and viscous-diffusion terms, also indicates the bandwidth of the scales of the turbulence processes. The turbulent Reynolds number, $Re_t = Re_0 E_K^2/\epsilon$ with $\epsilon = -\langle u_i \tau_{ij,j} \rangle$ is shown in figure 7. The maximum $Re_t$ attained by the flow increases as $Re_{b_0}$ or $Sc$ increase and varies between 30 for case 1Base to 2380 for case 2Re2. Note also that if the $Re_{b0}$ is small enough, there is no distinctive peak in the evolution of $Re_t$ (as happens for case 1) and the flow never fully undergoes transition before decaying. It is peculiar to see that the decay of energy is such that the turbulent Reynolds number remains approximately constant. This is also seen, for certain initial conditions, in the decay of constant density isotropic turbulence (Ristorcelli & Livescu 2004). Here, it appears to be due to the buoyancy production not stopping until the fluid is fully mixed.

For non-buoyant flows, nonlinear effects are typically neglected at small Reynolds numbers and different Fourier components of $\rho$ and $u_i$ behave independently and may be superimposed. For unstable VD flows, depending on the Froude number, velocity fluctuations can be quickly generated such that the nonlinear interactions become important. In addition, if the density has large-amplitude perturbations, nonlinear interactions between various modes occur for even small initial Reynolds numbers. Consider, for example, that the linear analysis for the RT problem is valid as long as $a\kappa \ll 1$, where $a$ and $\kappa$ are the initial amplitude and wavenumber of the interfacial perturbation (Chandrasekhar 1981). For the viscous case, $a\kappa$ is also proportional to the Reynolds number based on $\kappa$ and interface speed. The initial conditions considered here correspond to large blobs with $L_\rho \kappa$ of order 1, so that the flow is nonlinear from early times.

It may be useful to report a bulk Reynolds number (Cook & Dimotakis 2001; Ristorcelli & Clark 2004) to compare the current problem to RT simulations. We choose the velocity integral scale (which turbulence models are expected to

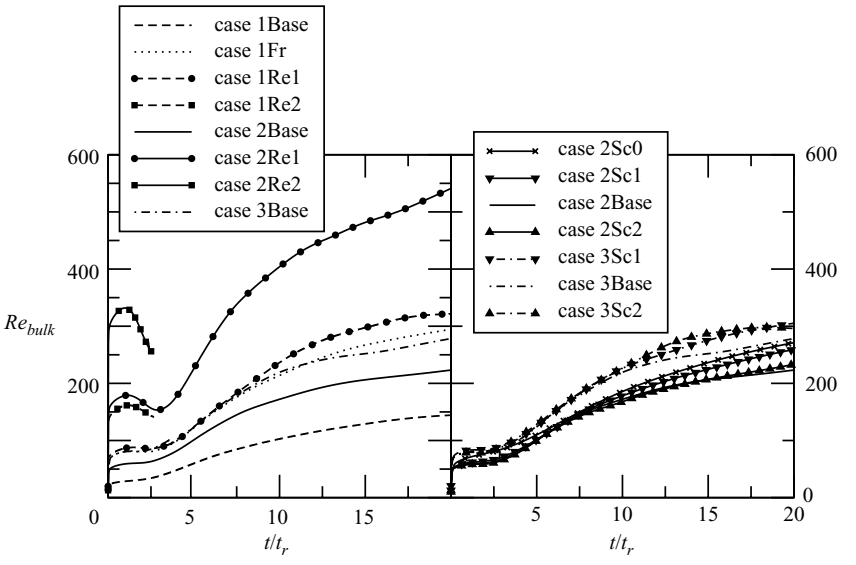


FIGURE 8. Time evolution of $Re_{bulk}$.

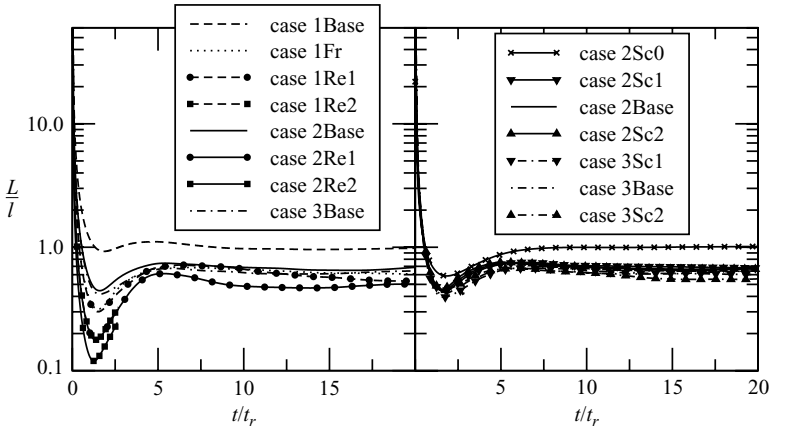


FIGURE 9. Time evolution of $L/l$.

compute) as the outer scale of the problem and define the bulk Reynolds number as $Re_{bulk} = (AgL)^{1/2}L/\nu$. This Reynolds number corresponds to the outer Reynolds number of Dimotakis (2000). In Boussinesq RT, $L \sim h$ as demonstrated in Ristorcelli & Clark (2004) using DNS and a self-similar analysis. The magnitude of $Re_{bulk}$ is dictated by the initial value of the buoyancy Reynolds number (figure 8). Since the evolution of $Re_{bulk}$ is dictated by the evolution of L, it decreases at early times for higher $Re_{b_0}$ cases as the stirring decorrelates the fluid motions. After the kinetic energy peaks, $Re_{bulk}$ increases monotonically and at late times the rate of growth decreases as the motions remain confined to the slowly decaying large-scale components of the motions. The shorter high-Reynolds-number simulations 1Re2 and 2Re2 attain maximum values of $Re_{bulk}$ of 162 and 302, respectively, before the kinetic energy peaks.

Single-point closures usually assume the validity of Kolmogorov's 'zeroth' law. It is useful to asses how the velocity integral length scale relates to the length scale $l = k^{3/2}/\epsilon$ (figure 9). It appears that during the transition process, before the energy maximum is

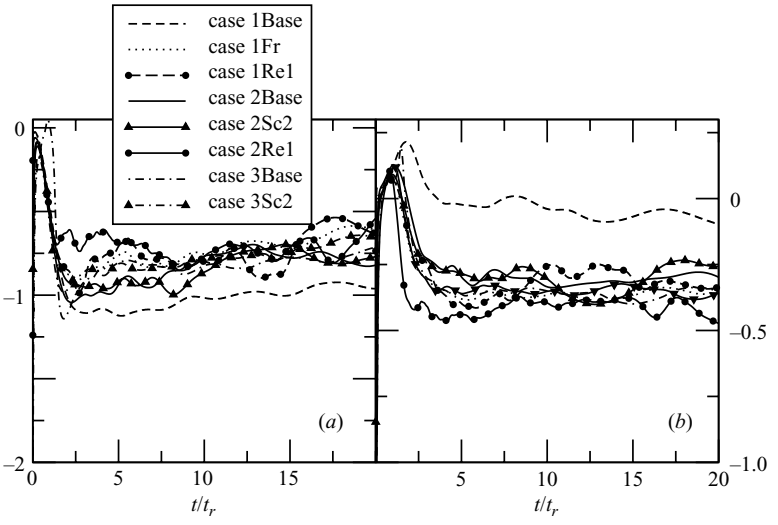


FIGURE 10. Derivative skewness ($a$) in the direction of gravity, $S_3 = \langle u_{3,3}^3 \rangle / \langle u_{3,3}^2 \rangle^{3/2}$, and ($b$) in the horizontal plane, $S_h = \frac{1}{2} \sum_{j=1,2} \langle u_{j,j}^3 \rangle / \langle u_{j,j}^2 \rangle^{3/2}$.

reached, the Kolmogorov zeroth law scaling is not useful. The scaling coefficient varies some two orders of magnitude. The effect appears to be a non-equilibrium effect as well as a VD effect. The scaling coefficient varies more as the Atwood number is increased. While many of the quantities presented have asymptotic behaviours that collapse with the buoyancy scaling, this is not the case with the Kolmogorov scaling coefficient. It is surprising that the zeroth law does hold, for each individual case, at long time.

The stabilization of the derivative skewness is often taken to indicate the development of the energy cascade. The derivative skewness varies significantly initially as the Reynolds number increases through transition. Figure 10 shows the evolutions of vertical and horizontal velocity derivative skewnesses. As the flow becomes Boussinesq-like, $S_3$ and $S_h$ reach values similar to those obtained in an RT layer for a Boussinesq fluid by Ristorcelli & Clark (2004) for all cases, except case 1Base. Note that the low $Re_{b0}$ case, even if it is Boussinesq from the beginning, achieves different long-time skewness statistics owing to the very low Reynolds numbers achieved during the evolution of the flow. This is, perhaps, an example of flow that does not go fully through transition.

### 4.2. *Energy transfer rates*

The rate of conversion of potential energy to kinetic energy is an important feature of buoyancy-driven flows. The sole mechanism by which the potential energy is converted to kinetic energy is the mass flux (as will be shown). In more conventional turbulent flows, the Reynolds stresses contracted on the mean velocity gradient extract energy from the mean velocity field at large scales and then the energy cascades down to small scales where it is viscously dissipated. Here, the potential energy of the unstable stratification is converted into kinetic energy by buoyancy forces. As a consequence, the kinetic energy is fed at a range of scales (as discussed in Livescu & Ristorcelli 2007).

The available potential energy per unit volume in a volume $\mathcal{V}$ for each realization is given by

$$E_p^*(t) = -\frac{g_i}{\mathcal{V}\, Fr^2} \int_{\mathcal{V}} (\rho^* - \overline{\rho})\, x_i \, \mathrm{d}\mathcal{V}. \tag{4.4}$$

Here the non-dimensional elevation $x_i$ varies from 0 to $2\pi$ in the direction opposite to $g_i$. $E_p^*(t)$ is the potential energy non-dimensionalized by $\rho_0 U_0^2$. In the fully mixed state, which corresponds to the stable configuration, $E_p^* = 0$.

The rate of change of the potential energy is the sum of the time rate of change of the potential energy inside the control volume and the flux of potential energy through the boundaries:

$$\mathscr{E}_{,t} = E^*_{p,t} + \mathcal{F}_{E_p^*}. \tag{4.5}$$

Using the definition of the potential energy (4.4), $\mathscr{E}_{,t}$ can be written as:

$$\begin{aligned}
\mathscr{E}_{,t} &= -\frac{\partial}{\partial t}\left(\frac{g_i}{\mathcal{V}\,Fr^2}\int_{\mathcal{V}}(\rho^* - \overline{\rho})\,x_i\,\mathrm{d}\mathcal{V}\right) - \frac{g_i}{\mathcal{V}\,Fr^2}\int_{\mathscr{S}} u_j(\rho^* - \overline{\rho})\,x_i \mathrm{d}\mathscr{S}_j \\
&= \frac{g_i}{\mathcal{V}\,Fr^2}\int_{\mathcal{V}}(\rho^* u_j)_{,j}\,x_i\,\mathrm{d}\mathcal{V} - \frac{g_i}{\mathcal{V}\,Fr^2}\int_{\mathscr{S}} u_j(\rho^* - \overline{\rho})\,x_i \mathrm{d}\mathscr{S}_j \\
&= -\frac{g_i}{\mathcal{V}\,Fr^2}\int_{\mathcal{V}}\rho^* u_i \mathrm{d}\mathcal{V} + \frac{g_i\overline{\rho}}{\mathcal{V}\,Fr^2}\int_{\mathscr{S}} u_j\,x_i \mathrm{d}\mathscr{S}_j \\
&= -\frac{g_i}{Fr^2}\langle\rho^* u_i\rangle + \frac{g_i\overline{\rho}}{\mathcal{V}\,Fr^2}\int_{\mathscr{S}} u_j\,x_i \mathrm{d}\mathscr{S}_j.
\end{aligned} \tag{4.6}$$

Here, (2.4) was used to eliminate the time derivative of the density. Integration by parts and the divergence theorem are then applied. The final term is obtained using the definition of the average and periodicity. Note that in general, for a particular realization and finite $\mathcal{V}$, the last surface integral term does not vanish. If (4.6) is averaged over independent realizations, then

$$\langle\mathscr{E}\rangle_{,t} = -\frac{g_i}{Fr^2}\langle\rho^* u_i\rangle. \tag{4.7}$$

Ergodicity has been assumed and thus the volume average of the mass flux remains unchanged after ensemble averaging.

The rate of change of kinetic energy per unit volume is obtained by multiplying the momentum equation (2.5) by $u_i$ and averaging:

$$E_{K,t} = \frac{g_i}{Fr^2}\langle\rho^* u_i\rangle + \langle p u_{j,j}\rangle - \langle u_{i,j}\tau_{ij}\rangle. \tag{4.8}$$

The first term, proportional to the mass flux, is precisely the rate of change of potential energy with opposite sign. The mass flux term represents the reversible transfer of energy between potential and kinetic forms. The mass flux is the sole mechanism by which the potential energy is converted into kinetic energy. The last two terms are the pressure dilatation and viscous dissipation. In compressible fluid flows, the pressure dilatation term represents the reversible transfer of energy between the kinetic and internal energies (Blaisdell, Mansour & Reynolds 1993; Ristorcelli 1997; Livescu *et al.* 2002). Here, it is the gain or loss of kinetic energy through work generated by the change of specific volume during mixing. For the simulations considered, $\langle p u_{j,j}\rangle$ is small except at the initial instant when it is the only non-zero term in the equation. After this initial instant, the two most important terms become the buoyancy production (proportional to the mass flux) and the viscous dissipation.

In contradistinction, for a Boussinesq fluid (see Appendix B) the rate of change of potential energy is:

$$\mathscr{E}_{,t} = -\frac{g_i}{\mathcal{V}\,Fr^2}\int_{\mathcal{V}}\left[\rho^* u_i - \frac{1}{Re_0 Sc}\rho^*_{,j}\right]\mathrm{d}\mathcal{V} + \frac{g_i}{\mathcal{V}\,Fr^2}\int_{\mathscr{S}}\left[\overline{\rho}u_j - \frac{1}{Re_0 Sc}\rho^*_{,j}\right]x_i \mathrm{d}\mathscr{S}_j, \tag{4.9}$$

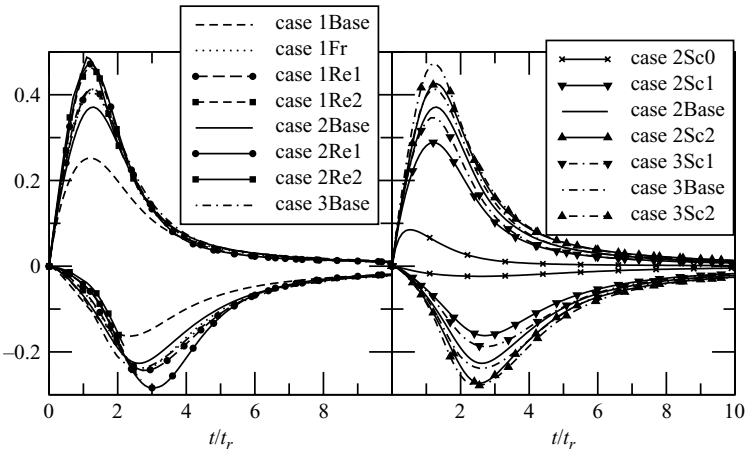


FIGURE 11. Time evolution of the terms in the kinetic energy equation (4.8) scaled by $\overline{\rho}U_r^2/t_r$. Production buoyancy term $P=(g_i/Fr^2)\langle\rho^* u_i\rangle$ upper curves, viscous term $-V=-\langle u_{i,j}\tau_{ij}\rangle$ lower curves.

while the rate of change of the kinetic energy is given by (4.8) with $\langle pu_{j,j}\rangle=0$. There is an additional irreversible loss of potential energy by molecular diffusion and additional diffusive transfer through the boundaries not present in the VD case. The Boussinesq approximation, unlike the VD case, allows molecular diffusion in the absence of fluid motion. While the point is generally important, it is not relevant to the homogeneous configuration, in which the extra diffusive terms in (4.9) vanish after ensemble averaging.

### 4.3. *Kinetic energy budget*

Figure 11 shows the evolution of the terms in the kinetic energy equation (4.8). Similar to the evolution of the kinetic energy, the buoyancy production term increases initially as the two fluids are accelerated, reaches a maximum and decreases as the fluids molecularly mix. As expected, the magnitude of the peak is larger if $A/Fr^2$ or $Re_0$ (or commensurately $Re_{b0}$) are increased (figure 11*a*). A similar behaviour is obtained for the evolution of the viscous dissipation. At late times, the results are similar for cases with the same $Sc$, suggesting that in the buoyancy force scaling they are only weakly influenced by $Re_{b_0}$. Since the results for cases 3Base and 1Fr with the same $A/Fr^2$ are close, figure 11 indicates that the mass flux itself has a weaker dependence on the acceleration due to gravity than on the Atwood number.

The production to dissipation ratio $R=P/\epsilon$ shown in figure 12 indicates the highly non-equilibrium nature of the flow. It is initially large, ranging from 24 for case 1 to 75 for case 2Re2. For clarity, the low $Sc$ cases are not shown in figure 12, but the results are consistent with the rest of the cases. At early times, $R$ is very different for the cases considered. After the energy reaches maximum, when $P=\epsilon$, the production dissipation ratios become similar, asymptoting to about a half. Apparently, a purely decaying turbulence is never attained; there is always a production mechanism. This is because the production is set by diffusive not viscous processes, and dissipation tracks the production.

### 4.4. *Favre mean and turbulent kinetic energies budgets*

The VD problem is more conveniently treated using Favre averages. The definitions are repeated here for convenience: $\overline{\rho}\tilde{U}_i=\langle\rho^* u_i^*\rangle$. Here $U_i=0$ and $\tilde{U}_i=a_i$, where $a_i=\langle\rho u_i\rangle/\overline{\rho}$. The Favre turbulent kinetic energy is $\overline{\rho}\tilde{k}=1/2\ R_{jj}$ where the Reynolds

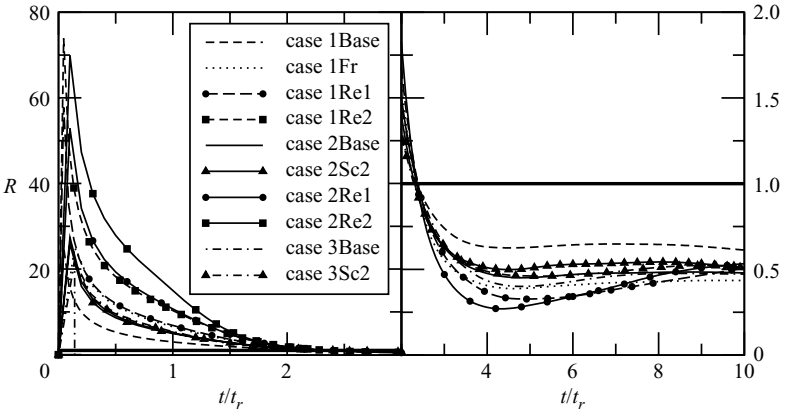


FIGURE 12. Production to dissipation ratio: (*a*) early time, (*b*) late time.

stresses are defined as $R_{ij} = \langle \rho^* u_i'' u_i'' \rangle$ with $u_i'' = u_i^* - \tilde{U}_i$. The relation between the Favre turbulent kinetic energy and the kinetic energy per unit volume, $E_K$, is $\overline{\rho}\tilde{k} = E_K - \tilde{K}$ where $\tilde{K} = \overline{\rho}\tilde{U}_i\tilde{U}_i/2$ is the Favre mean kinetic energy. Using (2.14) and the mean pressure gradient relation (2.17), the transport equations for $\tilde{K}$ and $\tilde{k}$ are:

$$\tilde{K}_{,t} = a_i \left[ \overline{\rho} \frac{g_i}{Fr^2} - P_{,i} \right], \tag{4.10}$$

$$\overline{\rho}\tilde{k}_{,t} = a_i P_{,i} + \langle p u_{j,j} \rangle - \langle u_{i,j} \tau_{ij} \rangle. \tag{4.11}$$

In a Favre average setting, the energy conversion is from potential to the Favre mean kinetic energy, $\tilde{K}$, by $(g_i/Fr^2)a_i\overline{\rho}$ and then to the Favre turbulent kinetic energy, $\tilde{k}$, by the production term $a_i P_{,i}$ (figure 13).

Note that the kinetic energy can be written as $E_K = 1/2\ (\overline{\rho}\langle u_i u_i \rangle + \langle \rho u_i u_i \rangle)$ and that $\overline{\rho}\tilde{k} = 1/2\ (\overline{\rho}\langle u_i u_i \rangle - \overline{\rho} a_i a_i + \langle \rho u_i u_i \rangle)$. For the cases considered here, $\overline{\rho} a_i a_i$ and $\langle \rho u_i u_i \rangle$ are small in comparison to $\overline{\rho}\langle u_i u_i \rangle$. The kinetic energy and Favre turbulent kinetic energy are almost equal to the kinetic energy per unit mass $\overline{\rho}\langle u_i u_i \rangle/2$. While the mass flux terms have small contributions to the Favre kinetic energies, the mass flux is the agency by which potential energy is converted to kinetic energy. More importantly, $a_i$ multiplies $P_{,i}$, a large term, to give the transfer between Favre mean and turbulent kinetic energies. The mass flux is probably the single most important item to predict in low-dimensional models if one needs to capture accurately the conversion of potential to kinetic energy. The rate of energy conversion dictates the growth rate of the RT mixing layer, so that there is a direct connection between the mass flux and the growth rate as observed by Cook *et al.* (2004), which further emphasizes the importance of the mass flux.

### 4.5. *Budget for the mass flux equation*

Having established the importance of the mass flux, it is useful to examine (2.14) more closely. The time evolution of the mass flux can be inferred from the kinetic energy production term, $(A/Fr^2)a_3\overline{\rho}$, shown in figure 11. Substituting for the mean pressure gradient (2.17), the mass flux equation can be written in either of the following two forms:

$$\overline{\rho} a_{i,t} = -\langle \rho v \rangle P_{,i} - \overline{\rho}(\langle u_i u_{j,j} \rangle - \langle v p_{,i} \rangle + \langle v \tau_{ij,j} \rangle), \tag{4.12}$$

$$\overline{\rho} a_{i,t} = -\frac{\overline{\rho}}{1 - \langle \rho v \rangle}(\langle \rho v \rangle \frac{g_i}{Fr^2} + \langle u_i u_{j,j} \rangle - \langle v p_{,i} \rangle + \langle v \tau_{ij,j} \rangle). \tag{4.13}$$

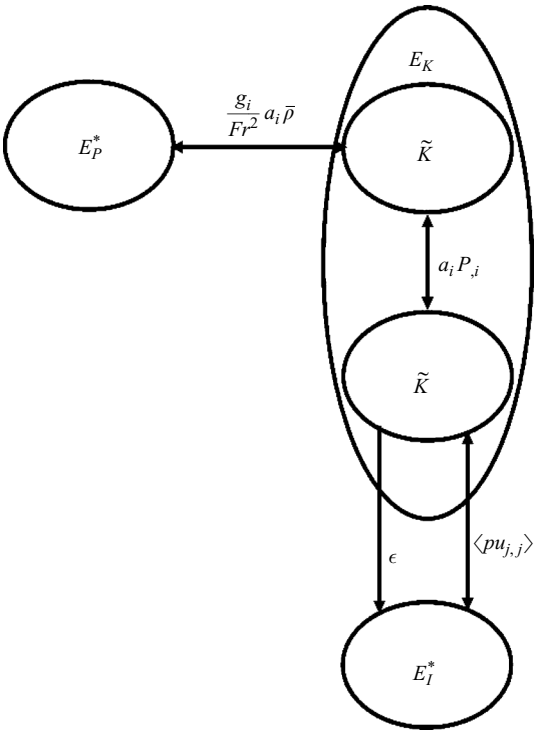


FIGURE 13. Energy transfers in variable-density turbulence.

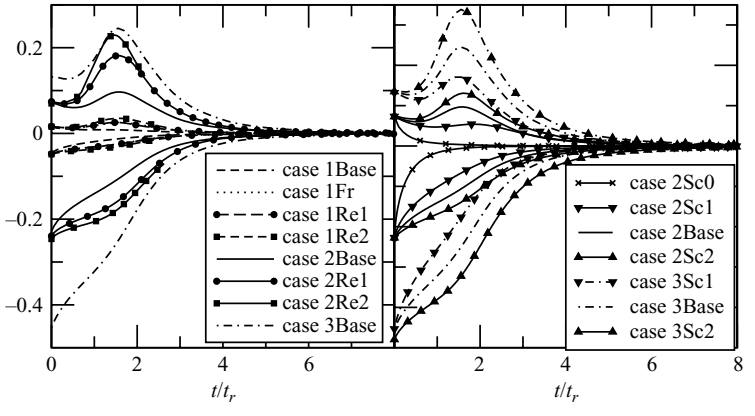


FIGURE 14. Terms in the mass flux transport equation (2.14) normalized by $U_r/t_r$. The positive terms correspond to $(\overline{\rho}/1 - \rho v)\langle v p_{,3} \rangle$ and the negative terms to $-(\overline{\rho}/1 - \langle \rho v \rangle)\langle \rho v \rangle (g_3/Fr^2)$.

The terms on the right-hand side of (4.13) are buoyancy production, velocity dilatation and specific volume pressure gradient and stress covariances. The density specific volume correlation is important since it controls the mass flux production. As $\langle \rho v \rangle$ tracks the mixing progress, it is discussed in the companion paper on mixing (Livescu & Ristorcelli 2007).

Figure 14 shows the two important terms in the equation, buoyancy production and specific volume pressure gradient correlation. Neither term is zero initially and

the mass flux is both generated and destroyed from the initial instant. Consistent with the results above, the terms in the mass flux equation increase their magnitude with $A$ or $Re_0$ or equivalently with the static initial Reynolds number $Re_{b0}$. Also, similar to the mass flux (see discussion above) the terms in figure 14 are less sensitive to changes in Froude number than in the Atwood number (compare cases 1, 3 and 4).

The buoyancy production directly depends on the density specific volume correlation, $\langle \rho v \rangle$, which changes during the evolution of the flow. In the Boussinesq approximation, there is no specific volume change and the mean pressure gradient is the hydrostatic head. If that were the case here, then (4.13), which is written as $\overline{\rho} a_{i,t} = -P_{,i} + \overline{\rho} g_i / Fr^2$, would predict a constant mass flux. For comparison, the mass flux equation for a Boussinesq fluid is given in (B 5). This emphasizes that in VD turbulence, the mean pressure gradient is a dynamical variable evolving as the mixing progresses.

## 5. Discussion and summary

An overview of the evolution of the buoyantly driven flow and its dependence on various parameters is now given. Then some issues on moment closure modelling are briefly discussed. The section ends with a short amplification of the differences between the current simulations and the problem studied by Batchelor *et al.* (1992).

In this homogeneous configuration, the turbulence is initiated by the action of the body force, increases as the buoyancy forces dominate at early times, and then decays as the viscous forces overcome the buoyancy forces. Unlike the RT configuration, there is no continuous supply of fresh fluid and the molecular mixing reduces the buoyancy production at late times. For cases with the same Schmidt number, there is an excellent collapse of the data with the time and velocity scalings that reflect a nonlinear to buoyancy force balance:

$$t_r = \sqrt{Fr^2/A}, \qquad U_r = \sqrt{A/Fr^2}, \tag{5.1}$$

where $Fr^2 \sim 1/g$ scales the gravity. In scaled time, the point where $P = \varepsilon$ collapses for all cases at $t/t_r \approx 2.5$.

(*a*) The initial conditions are characterized by an initial static Reynolds number,

$$Re_{b0} = Re_0 \sqrt{L_\rho^3 A / Fr^2}, \tag{5.2}$$

which plays an important role in setting the rate of growth of the kinetic energy and turbulent Reynolds number and the size of the kinetic energy maxima. There appears to be a critical $Re_b$ (dependent on $Sc$) above which additional increase in $Re_{b0}$ has little effect on the flow. This is likely to be the case for the RT layer as well (see Cabot & Cook 2006). For the higher-Atwood-number simulations, the fluid has not mixed (molecularly) enough by the time the peak energy occurs and the fluid is still non-Boussinesq. The non-Boussinesq behaviour also persists longer at higher Schmidt numbers.

The Schmidt number also affects the magnitude of the kinetic energy maximum: the higher the Schmidt number, the larger the peak. The Schmidt number does not affect the time of the energy maxima.

During the early time transition period none of the usual statistics, the derivative skewness or the scaling of the integral length scale with $\ell = k^{3/2}/\epsilon$, behave as seen in non-buoyant fully developed turbulence. During this time, the anisotropy is largest

and the non-equilibrium measure, the production dissipation ratio, is as high as $P/\varepsilon \sim 70$ as the flow goes through transition.

(*b*) At the time of kinetic energy maximum, when $P = \varepsilon$, the r.m.s. density fluctuations are large and the mean pressure gradient is not hydrostatic. It is also at this time that any unmixed pure fluid is rare and the density PDF loses its bimodal structure as pure fluid mixes, but has not yet developed a quasi-Gaussian single peak characteristic of long-term mixing (see Livescu & Ristorcelli 2007 for details). At this time, the derivative skewness is approaching values taken to be symptomatic of a fully developed cascade and the Kolmogorov zeroth law scaling of the integral length scale with $\ell = k^{3/2}/\epsilon$ becomes useful.

(*c*) At late time, after $t/t_r \approx 2.5$ the production is smaller than the dissipation and the asymptotic decay is set by the molecular diffusion which controls the mixing and determines the energy production. The decay occurs with an approximately constant production dissipation ratio, $P/\varepsilon \approx 0.5$. A similar equilibration of dissipation to production occurs on the centreline of the long-time Boussinesq RT layer (Ristorcelli & Clark 2004).

### 5.1. *Modelling issues*

The mass flux appears to be the most important quantity to predict in lower-dimensional models to accurately simulate the highly non-equilibrium portion of the flow evolution. The conversion of potential to kinetic energy is accomplished, at all scales of motion, by the mass flux. An interesting question is then whether the energy cascade has a constant flux or what an inertial range looks like. It appears likely that special care may have to be taken with the choice and development of LES subgrid closures.

While 'mass flux' connotes a transport quantity, it should be kept in mind that in this flow the mean density gradient is zero. The mass flux is a unique dynamical variable not related to the mean density gradient as simplistic gradient transport models assume in self-similar turbulence flows.

For validating engineering and moment closures, the following measures appear most useful for assessing the accuracy and utility of the modelling during the different stages of flow evolution.

(*a*) The non-dimensional time at which the kinetic energy peaks and at which $P = \varepsilon$, for the initial length scales chosen, is always $t/t_r \approx 2.5$.

(*b*) The early time and late time $P/\varepsilon$ ratio.

(*c*) The early time overshoot and post peak relaxation of the mean pressure gradient to the hydrostatic value.

(*d*) The dependence of all these parameters and the magnitude of the kinetic energy on the initial $Re_b$.

(*e*) As many applications of moment closures or ILES apply to the inviscid limit and do not define a viscosity, the eddy turnover time, $k/\varepsilon$, and the turbulent eddy viscosity, $k^2/\varepsilon$, are given in the figures 15 and 16 for model validation.

The scaling of the integral length scale with $\ell = k^{3/2}/\epsilon$ – the so-called Kolmogorov's zeroth law – does hold, with non-unique coefficient of proportionality, once the turbulence starts to decay. It is not clear that the non-equilibrium nature of the flow, the low Reynolds number or non-Boussinesq effects are responsible for the absence of the zeroth law scaling before the decay begins. It appears to be probably due to all three effects.

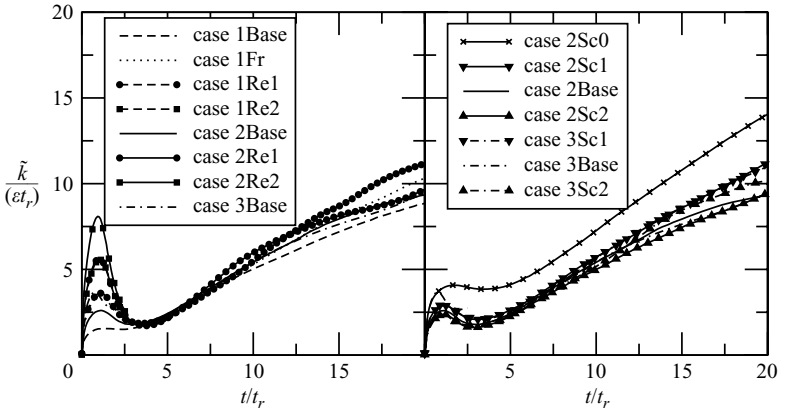


FIGURE 15. Time evolution of the normalized eddy turnover time, $\tilde{k}/\varepsilon$.

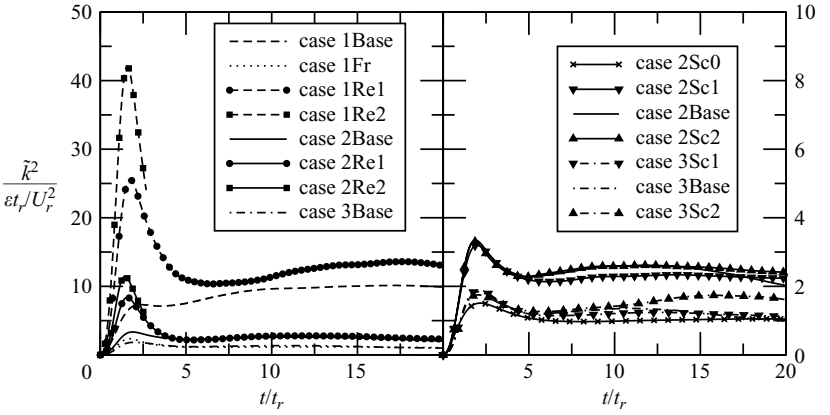


FIGURE 16. Time evolution of the normalized turbulent eddy viscosity, $\tilde{k}^2/\varepsilon$.

The list above deals with hydrodynamical related quantities. Mixing-related predictables are given in Livescu & Ristorcelli (2007).

### 5.2. *Contrasting the initial-value problem with the Batchelor treatment*

For the Boussinesq problem, Batchelor *et al.* (1992) found non-trivial similarity states in the decay stage that depend on the infrared properties of the initial buoyancy spectrum. At all times, the energy in the density modes with $\kappa \to 0$ becomes small (see Appendix B). Moreover, even for the large-Atwood cases, the density fluctuations decrease at late times and the Boussinesq approximation becomes valid. Therefore, similar infrared spectral properties might be expected in the current VD simulations. Whether this leads to self-similar regimes seen in the Boussinesq case is not addressed in this paper. Here, the initial density spectrum is a top hat corresponding, in physical space, to several large blobs. As a consequence, the low-wavenumber exponent changes in time as the lowest wavenumbers are filled with energy and arguments such as those given in Batchelor *et al.* (1992) relating decay rate to the infrared exponent are not germane. All simulations presented have the same initial spectrum of density fluctuations and as a consequence, the well-known low-wavenumber dependence of

the asymptotic state is likely to have been suppressed. Conclusions regarding the similarity of the different asymptotic state reflect the dependence on the dynamical balances of the equations and not the energy in the low-wavenumber spectra.

## 6. Conclusions

Simulations of the benchmark problem of homogeneous buoyantly driven VD turbulence have allowed us to study the coupling between the scalar mixing and hydrodynamics. The current study has been designed to have the largest mass flux possible and is the maximally non-equilibrium flow possible. Flows with Atwood number up to $A = 0.5$, density variations as large as half the mean density, $\rho_{rms} = 0.5\bar{\rho}$, for Schmidt numbers $0.1 \leqslant Sc \leqslant 2$ have been studied. This study has focused on the hydrodynamics; the material mixing is studied in the companion paper (Livescu & Ristorcelli 2007).

The simulations have been motivated by the absence of data relevant to moment closures or LES developments in VD turbulence that capture the core nonlinear couplings between material mixing and the fluctuating hydrodynamical field in the absence of the complicating issues of spatial transport. In this buoyantly driven study, the usual quadratic nonlinearities as well as new cubic nonlinearities associated with the material mixing are important. The simulations include: (i) the highly anisotropic non-equilibrium transition process starting at negligible Reynolds number and in which production vastly exceeds dissipation; (ii) a nominally high-Reynolds-number portion in which production matches dissipation; and (iii) an anisotropic decay stage in which production is about half the dissipation. It is useful to view this benchmark flow as characteristic of the interior of a fully developed RT layer.

The results of our study of buoyantly driven VD transition and turbulence allows the following list of findings and generalizations.

1. The mass flux is probably the single most important dynamical quantity taht it is necessary to predict in low-dimensional models in order to reflect the conversion of potential to kinetic energy accurately. The $a_i P_{,i}$ product determines the growth of the Favre turbulent kinetic energy and thus the highly non-equilibrium transition process. This is also the case for the VD form of the RT problem. Despite the importance of the mass flux in setting the energetics of the flow, it does not make much contribution to the Favre kinetic energy, $R_{kk}$. The mass flux is its own dynamical variable and not linked to any mean flow variables as it is in simplistic gradient transport arguments that make it proportional to the mean density gradient.

2. The mean pressure gradient in VD turbulence is not hydrostatic as it is for a Boussinesq fluid; it is a dynamically evolving quantity. The mean pressure gradient is intimately coupled to material mixing through the specific volume pressure correlation (Sandoval *et al.* 1996; Livescu & Ristorcelli 2007). Once enough mixing has taken place so that $\langle vp_{,i} \rangle$ is negligible, the fluid becomes a Boussinesq fluid and the mean pressure gradient is hydrostatic. Thus, $\langle vp_{,i} \rangle$ is responsible for the non-Boussinesq behaviour of the mean pressure gradient and this is most important during the early-time transition process. The period over which the fluid is non-Boussinesq, as measured by the density variance, can be prolonged according to the magnitude of the Schmidt number. The period over which the fluid is non-Boussinesq, as measured by $\langle vp_{,i} \rangle$, does not appear as sensitive to the Schmidt number. Even during the time the flow is non-Boussinesq, some integral quantities still seem to obey Boussinesq scalings (e.g. the $\rho_{rms}/(\rho_2 - \rho_1)$ becomes dependent on $Re_{b_0}$ and $Sc$ only at early times; at late times, $Sc$ becomes the only parameter).

3. There are important material diffusion effects, as made clear by the Schmidt-number effect. In the buoyancy-nonlinear scalings, the most important Schmidt-number effect is on the rate of dissipation of the material fluctuations and thus the rapidity in which the fluid transitions from a VD fluid to a Boussinesq-like fluid then to a homogeneous mixture. This point is more evident in the PDF of the material field shown in Livescu & Ristorcelli (2007).

4. The short-time evolution and transition of the flow is dependent on the static initial Reynolds number that sets the maximum kinetic energy attained. This is also seen in RT flows and in the Boussinesq fluid of Batchelor *et al.* (1992). It is observed that the higher the initial $Re_{b0}$, the faster the mixing occurs. This is a reminder of the effect observed in Cook *et al.* (2004). In scaled time, the kinetic energy maxima occur at approximately the same time, ($\approx$2.5), for all simulations regardless of $Re_{b_0}$ or $Sc$.

5. An improved pressure projection algorithm useful for VD flow simulations has been constructed. The algorithm allows the computations without introducing additional temporal discretization errors in the pressure step.

The density fluctuations are initially some 50% of the mean density for the highest-Atwood-number case presented. The importance of the non-Boussinesq nature of the fluid as affected by Atwood and Schmidt numbers is clearly indicated by these 'modestly' non-Boussinesq exploratory simulations. For the higher-Atwood-number runs, the flow is non-Boussinesq past the peak of the kinetic energy as moderated by the Schmidt number.

Higher-Atwood-number simulations are difficult to perform for the relatively thin initial diffusion layers and large blob configuration considered here. The initial diffusion layer between the fluids becomes squeezed by the motion of the pure fluid blobs and significantly increases the resolution requirements. In any event, it is possible to report, from a few short runs with wider initial diffusion layers, that different flow hydrodynamics appears to occur at large Atwood numbers. This is reminiscent of the divergence in behaviour that we see between the bubble and spike sides observed in the RT layer for $A \geqslant 0.5$ in the compendium by Dimonte & Schneider (2000). The mixing problem is also very different at low versus high Atwood numbers (specifically radically different behaviour in light versus heavy fluids) and this is presented and explored in Livescu & Ristorcelli (2007).

Computational resources were provided through the Institutional Computing Project, Los Alamos National Laboratory. This work was performed under the auspices of US Department of Energy.

## Appendix A. Numerical method

The numerical method for solving the governing equations is now explained. The method requires a solution for the pressure from the VD Poisson equation. A new approach is derived and explained. The new method preserves the overall order of the method and ensures that (2.6), which gives the divergence of the velocity, is 'exactly' satisfied.

In non-dimensional form, the continuity (in terms of the logarithm of the density) and the fluctuating momentum transport equations are:

$$\ln(\rho^*)_{,t} = -u_j \ln(\rho^*)_{,j} + \frac{1}{ReSc} \ln(\rho^*)_{,jj}, \tag{A 1}$$

$$(\rho^* u_i)'_{,t} = -(\rho^* u_i u_j)_{,j} - p_{,i} + \tau_{ij,j} + \frac{1}{Fr^2} \rho g_i, \tag{A 2}$$

The continuity equation is integrated using a second-order-accurate Adams–Bashforth method:

$$\ln(\rho^*)^{n+1} = \Delta t(1.5A^n - 0.5A^{n-1}) + O(\Delta t^3), \tag{A 3}$$

where $A$ is the right-hand side of (A 2). The fluctuating momentum equation is rewritten as

$$(\rho^* u_i)'_{,t} = -p_{,i} + B_i, \tag{A 4}$$

and integrated from $t^n$ to $t^{n+1}$

$$\frac{(\rho^* u_i)'^{\,n+1} - (\rho^* u_i)'^n}{\Delta t} = -\tilde{p}_{,i} + \frac{1}{\Delta t}\int_{t^n}^{t^{n+1}} B_i \,\mathrm{d}t, \tag{A 5}$$

where $\tilde{p} = (1/\Delta t)\int_{t^n}^{t^{n+1}} p \,\mathrm{d}t$ and the last term in the equation is evaluated via the Adams–Bashforth method:

$$\int_{t^n}^{t^{n+1}} B_i \,\mathrm{d}t = \Delta t(1.5B^n - 0.5B^{n-1}) + O(\Delta t^3). \tag{A 6}$$

The fluctuating momentum equation is integrated in two steps, first without the pressure terms:

$$(\rho^* u_i)'^{\,n+1/2} = (\rho^* u_i)'^{\,n} + \Delta t(1.5B^n - 0.5B^{n-1}) + O(\Delta t^3). \tag{A 7}$$

In the second step, the pressure terms are added:

$$(\rho^* u_i)'^{\,n+1} = (\rho^* u_i)'^{\,n+1/2} - \Delta t\,\tilde{p}_{,i}. \tag{A 8}$$

Note that summing (A 7)–(A 8) results in (A 5). The Poisson equation for pressure is obtained by taking the divergence of (A 8):

$$\tilde{p}_{,ii} = -\frac{1}{\Delta t}\left[(\rho^* u_i)'^{\,n+1}_{,i} - (\rho^* u_i)'^{\,n+1/2}_{,i}\right]. \tag{A 9}$$

Equation (A 9) contains the unknown divergence of the momentum at the next time step, which must be evaluated in order to be able to calculate the pressure. One method, developed by McMurtry (1987), is to use the continuity equation and write $(\rho u_i)'^{\,n+1,}_i$ in terms of the time derivative of the density which is approximated using a second-order backward difference. Such an approximation becomes unstable at large density fluctuations as shown by Sandoval (1995). A more robust method was developed by Sandoval (1995) and also used for RT simulations by Cook & Dimotakis (2001). In this method, $(\rho u_i)'^{\,n+1}_{,i}$ is expanded as:

$$\begin{aligned}(\rho^* u_i)'^{\,n+1}_{,i} &= \left[(\rho^* u_i)'^{\,n+1} + \langle \rho^* u_i \rangle^{n+1}\right]_{,i} \\ &= \left(\rho^{*\,n+1} u_i^{n+1}\right)_{,i} = u_i^{n+1}\rho^{*\,n+1}_{,i} - \frac{1}{Re_0 Sc}\rho^{*\,n+1}(\ln \rho^{*\,n+1})_{,ii}.\end{aligned} \tag{A 10}$$

In (A 10), the zero spatial derivative of the mean momentum is used to obtain the first equality and (2.6) is used to derive the last equality. An expression for $u_i^{n+1}$ is required to close the divergence of the momentum. Following Sandoval (1995), a Taylor series expansion is used to obtain:

$$u_i^{n+1} = 2u_i^n - u_i^{n-1} + O(\Delta t^2). \tag{A 11}$$

The approximation (A 11) is unfortunately second-order accurate and could affect the overall accuracy if a higher-order scheme is used for the first step or the mass

conservation. There is, however, an exact alternative. Instead of using (A 11), $u_i^{n+1}$ can be written exactly:

$$u_i^{n+1} = \frac{\rho^{*\,n+1} u_i^{n+1}}{\rho^{*\,n+1}} = \frac{1}{\rho^{*\,n+1}}[(\rho^* u_i)'^{\,n+1} + \langle \rho^* u_i \rangle^{n+1}]. \tag{A 12}$$

Equation (2.18) is used to eliminate $\langle \rho^* u_i \rangle^{n+1}$ and (A 8) to eliminate $(\rho^* u_i)'^{\,n+1}$ so that $u_i^{n+1}$ is given by

$$u_i^{n+1} = \frac{1}{\rho^{*\,n+1}} \left[ (\rho^* u_i)'^{\,n+1/2} - \Delta t \tilde{p}_{,i} - \frac{\langle v^{n+1}[(\rho^* u_i)'^{\,n+1/2} - \Delta t \tilde{p}_{,i}] \rangle}{V^{n+1}} \right]. \tag{A 13}$$

Using (A 13) in (A 10), closes exactly $(\rho^* u_i)'^{\,n+1}_{,i}$ appearing in (A 9). The numerical Poisson equation (A 9) becomes:

$$\left( \frac{\tilde{p}_{,i}}{\rho^{*\,n+1}} \right)_{,i} = \frac{1}{\Delta t} \left\{ \frac{1}{Re_0 Sc} (\ln \rho^{*\,n+1})_{,ii} + \left[ \frac{(\rho^* u_i)'^{\,n+1/2}}{\rho^{*\,n+1}} \right]_{,i} - \left( \frac{1}{\rho^{*\,n+1}} \right)_{,i} \times \frac{\langle v^{n+1} (\rho^* u_i)'^{\,n+1/2} \rangle}{V^{n+1}} \right\} + \left( \frac{1}{\rho^{*\,n+1}} \right)_{,i} \frac{\langle v^{n+1} \tilde{p}_{,i} \rangle}{V^{n+1}}. \tag{A 14}$$

In Fourier modes, the equation for pressure becomes:

$$\begin{aligned} \tilde{p} = {} & \frac{\rho^{n+1}}{\Delta t Re_0 Sc} \\ & - \frac{1}{\Delta t} \mathcal{F}^{-1} \left\{ \frac{\mathrm{i} k_i}{k^2} \mathcal{F} \left[ \rho^{n+1} \left( \mathcal{F}^{-1} \left( \frac{k_i k_j}{k^2} \left[ \mathcal{F} \left( \frac{(\rho^* u_i)'^{\,n+1/2}}{\rho^{*\,n+1}} \right) \right. \right. \right. \right. \\ & \left. \left. \left. \left. - \mathcal{F} \left( \frac{1}{\rho^{n+1}} \right) \frac{\langle v^{n+1}[(\rho^* u_i)'^{\,n+1/2} - \Delta t \tilde{p}_{,i}] \rangle}{V^{n+1}} \right] \right) + \Delta t \langle v^{n+1} \tilde{p}_{,i} \rangle \right) \right] \right\}, \end{aligned} \tag{A 15}$$

where $\mathcal{F}$ and $\mathcal{F}^{-1}$ represent Fourier and inverse Fourier transforms. There is still a closure problem in (A 15): the pressure appears in the angle brackets on the right-hand side. This is resolved as follows. Take the derivative in the $i$ direction, multiply by the fluctuating specific volume $v$ and average. A linear equation with known coefficients for $\langle v^{n+1} \tilde{p}_{,i} \rangle$ is obtained, whose solution is used to close the right-hand side of (A 15) which allows the determination of the instantaneous pressure. This approach preserves the order of accuracy of the first integration step, (A 7). As we might expect, the procedure increases the computational effort. For the Adams–Bashforth method used here, the procedure is more robust than the approximation (A 11) at large Atwood numbers. If the condition $U_i = 0$ is not imposed and the full momentum equation integrated, as is done in non-periodic VD flows, the Poisson equation (A 14) becomes:

$$\left( \frac{\tilde{p}_{,i}}{\rho^{*\,n+1}} \right)_{,i} = \frac{1}{\Delta t} \left\{ \frac{1}{Re_0 Sc} (\ln \rho^{*\,n+1})_{,ii} + \left[ \frac{(\rho^* u_i^*)^{\,n+1/2}}{\rho^{*\,n+1}} \right]_{,i} \right\}. \tag{A 16}$$

The computational effort necessary to solve (A 16) is close to that required by the usual Poisson equation using the (A 11) truncation.

## Appendix B. Small Atwood limit

For small Atwood numbers, the Boussinesq approximation is usually used for RT calculations. The approximation assumes that the density variations are small ($\rho \ll \overline{\rho}$)

and affect the flow through the buoyancy term only (Batchelor *et al.* 1992). Density variations can be seen as linearly depending on some conserved scalar property of the fluid $\rho = \beta\Phi$ (where $\Phi$ can be, for example, concentration or temperature) and the Boussinesq equations are:

$$u^*_{j,j} = 0, \tag{B 1}$$

$$u^*_{i,t} + u^*_j u^*_{i,j} = -p_{,i} + \frac{1}{Re_0} u^*_{,jj} + \frac{1}{Fr^2}\rho g_i, \tag{B 2}$$

$$\rho_{,t} + u^*_j \rho_{,j} = \frac{1}{Re_0 M}\rho_{,jj}, \tag{B 3}$$

where $M$ is the non-dimensional number which expresses the ratio of the diffusivity of momentum and diffusivity of $\Phi$ (e.g. $M = Pr$ if $\Phi$ is the temperature). Equation (B 1) follows from the continuity equation, if the quadratic diffusive term is neglected compared to the right-hand side in (B 3), (B 2) is the momentum equation, and (B 3) is the transport equation for the scalar $\Phi$ with $\Phi$ replaced by $\rho/\beta$. In the momentum equation, the mean pressure gradient is assumed equal to the pressure head $(1/Fr^2)\overline{\rho} g_i$ and was subtracted from the buoyancy term. In order to obtain (B 2) from (2.5), first (2.5) is divided by $\rho^*$ after the left-hand side is expanded with the use of the continuity equation. Then, it is assumed that $1/\rho^* = 1/\overline{\rho}(1-\rho/\overline{\rho}) + \cdots \approx 1/\overline{\rho}$. This is a zero-order approximation in $\rho/\overline{\rho}$ which also implies $V \approx 1/\overline{\rho}$ and $1/V\langle v(p_{,i} - \tau_{ij,j})\rangle \ll (p_{,i} - \tau_{ij,j})$. By comparing (B 1) and (2.6), it can be seen that the velocity divergence remains non-zero, even if (B 3) is assumed valid. Nevertheless, for large $Re_0 Sc$, it can be assumed that the contributions from the dilatational component to the convective term and the viscous stress tensor are negligible in comparison to those of the solenoidal part, so that replacing the mean pressure gradient given by (2.17) in (2.5) leads to (B 2).

In the continuity equation, the term $-\rho_{,j}\rho_{,j}/\rho^*$ is neglected in comparison to $\rho_{,jj}$. This is a valid approximation for small density fluctuations and a smooth density field. If, however, the density field is not smooth, there may be regions in the flow where the approximation is not valid. In spectral space, the approximation above becomes valid, even at large $At$ numbers, at both ends of the buoyancy spectrum where the energy content decreases to zero. The high-wavenumber range, however, presents an additional complication since the dilatational kinetic energy, as it is set by density gradients, can become comparable with the solenoidal part.

Also note that the VD continuity equation can be written as an advection–diffusion equation with an effective velocity equal to the solenoidal velocity $u_i^{eff} = u_i + (1/Re_0 Sc)(\rho^*_{,i}/\rho^*)$ as the advection velocity. In this case, the equation is formally the same as the continuity equation for the Boussinesq approximation with advective velocity $u_i^{eff}$.

For a Boussinesq fluid, the rate of change of potential energy is:

$$\begin{aligned}
\mathscr{E}_{,t} &= E^*_{p,t} - \frac{g_i}{Fr^2}\int_{\mathscr{S}} u_j(\rho^* - \overline{\rho})\, x_i \mathrm{d}\mathscr{S}_j \\
&= \frac{g_i}{Fr^2}\int_{\mathscr{V}} \left[\rho^*_{,j} u_j + \frac{1}{Re_0 Sc}\rho^*_{,jj}\right] x_i \,\mathrm{d}\mathscr{V} - \frac{g_i}{Fr^2}\int_{\mathscr{S}} u_j(\rho^* - \overline{\rho})\, x_i \mathrm{d}\mathscr{S}_j \\
&= -\frac{g_i}{Fr^2}\int_{\mathscr{V}} \left[\rho^* u_i - \frac{1}{Re_0 Sc}\rho^*_{,j}\right] \mathrm{d}\mathscr{V} + \frac{g_i}{Fr^2}\int_{\mathscr{S}} \left[\overline{\rho} u_j - \frac{1}{Re_0 Sc}\rho^*_{,j}\right] x_i \mathrm{d}\mathscr{S}_j.
\end{aligned} \tag{B 4}$$

This formula could be derived directly from the VD result (4.6) by splitting the velocity into solenoidal and dilatational parts. Like the VD case, the potential energy

is converted into kinetic energy by a term proportional to the mass flux. However, unlike the VD case (4.13), the production of the mass flux is mediated by the density variance, as:

$$\overline{\rho}a_{i,t} = \frac{\langle\rho^2\rangle g_i}{Fr^2} - \langle\rho p_{,i}\rangle - \left(\frac{1}{Re_0} + \frac{1}{Re_0 Sc}\right)\langle\rho_{,j}u_{i,j}\rangle. \tag{B 5}$$

## REFERENCES


Batchelor, G. K., Canuto, V. M. & Chasnov, J. R. 1992 Homogeneous buoyancy-generated turbulence. *J. Fluid Mech.* **235**, 349–378.

Besnard, D., Harlow, F. H., Rauenzahn, R. M. & Zemach, C. 1992 Turbulence transport equations for variable-density turbulence and their relationships to two field models. *Tech. Rep*. Los Alamos National Laboratory, lA-12303-MS.

Blaisdell, G. A., Mansour, N. N. & Reynolds, W. C. 1993 Compressibility effects on the growth and structure of homogeneous turbulent shear flows. *J. Fluid Mech.* **256**, 443–485.

Cabot, W. H. & Cook, A. W. 2006 Reynolds number effects on Rayleigh–Taylor instability with possible implications for type-ia supernovae. *Nature Phys.* **2**, 562–568.

Chandrasekhar, S. 1981 *Hydrodynamic and Hydromagnetic Stability*. Dover.

Cook, A. W. & Dimotakis, P. E. 2001 Transition stages of Rayleigh–Taylor instability between miscible fluids. *J. Fluid Mech.* **443**, 69–99.

Cook, A. W., Cabot, W. H. & Miller, P. L. 2004 The mixing transition in Rayleigh–Taylor instability. *J. Fluid Mech.* **511**, 333–362.

Dalziel, S. B., Linden, P. F. & Youngs, D. L. 1999 Self-similarity and internal structure of turbulence induced by Rayleigh–Taylor instability. *J. Fluid Mech.* **399**, 1–48.

Dimonte, G. & Schneider, M. 2000 Density ratio dependence of Rayleigh–Taylor mixing for sustained and impulsive acceleration histories. *Phys. Fluids* **12**, 304–321.

Dimotakis, P. E. 2000 The mixing transition in turbulent flows. *J. Fluid Mech.* **409**, 69–98.

Eswaran, V. & Pope, S. B. 1988 Direct numerical simulations of the turbulent mixing of a passive scalar. *Phys. Fluids* **31**, 506–520.

Givi, P. 1989 Model-free simulations of turbulent reacting flows. *Prog. Energy Combust. Sci.* **15**, 1–107.

Jang, Y. & de Bruyn Kops, S. M. 2007 Pseudo-spectral numerical simulation of miscible fluids with a high density ratio. *Comput. Fluids* **36**, 238–247.

Karniadakis, G. E., Israeli, M. & Orszag, S. A. 1991 High-order splitting methods for the incompressible Navier–Stokes equations. *J. Comput. Phys.* **97**, 414–2719.

Livescu, D. & Ristorcelli, J. R. 2007 Variable density mixing in buoyancy-driven turbulence. *J. Fluid Mech.* (submitted).

Livescu, D., Jaberi, F. A. & Madnia, C. K. 2002 The effects of heat release on the energy exchange in reacting turbulent shear flow. *J. Fluid Mech.* **450**, 35–66.

McMurtry, P. A. 1987 Direct numerical simulation of a reacting mixing layer with chemical heat release. PhD thesis, University of Washington.

Ristorcelli, J. R. 1997 A pseudo-sound constitutive relationship for the dilatational covariances in compressible turbulence: an analytical theory. *J. Fluid Mech.* **347**, 37–70.

Ristorcelli, J. R. & Clark, T. T. 2004 Rayleigh-Taylor turbulence: self-similar analysis and direct numerical simulations. *LANL Rep. 03-4273* and *J. Fluid Mech.* **507**, 213–253.

Ristorcelli, J. R. & Livescu, D. 2004 Decay of isotropic turbulence: fixed points and solutions for nonconstant $G \sim R_\lambda$ palinstrophy. *Phys. Fluids* **16**, 3487–3490.

Ristorcelli, J. R. & Livescu, D. 2007 Second-order moment modelling of buoyantly driven variable density turbulence. In preparation.

Sandoval, D. L. 1995 The dynamics of variable density turbulence. PhD thesis, University of Washington *LANL Rep.* LA-13037-T.

Sandoval, D. L., Clark, T. T. & Riley, J. J. 1996 Buoyancy-generated variable density turbulence. In *Proc. IUTAM Symp. on Variable Density Low Speed Turbulent Flows*, pp. 847–864. Kluwer.

Young, Y. N., Tufo, H., Dubey, A. & Rosner, R. 1999 On the miscible Rayleigh–Taylor instability: two and three dimensions. *J. Fluid Mech.* **447**, 377–408.